



**HAL**  
open science

# Shattering and growth of cold clouds in galaxy clusters: the role of radiative cooling, magnetic fields, and thermal conduction

Fred Jennings, Ricarda S. Beckmann, Debora Sijacki, Yohan Dubois

► **To cite this version:**

Fred Jennings, Ricarda S. Beckmann, Debora Sijacki, Yohan Dubois. Shattering and growth of cold clouds in galaxy clusters: the role of radiative cooling, magnetic fields, and thermal conduction. *Monthly Notices of the Royal Astronomical Society*, 2023, 518, pp.5215-5235. 10.1093/mnras/stac3426 . insu-03947316

**HAL Id: insu-03947316**

**<https://insu.hal.science/insu-03947316>**

Submitted on 12 Jul 2023

**HAL** is a multi-disciplinary open access archive for the deposit and dissemination of scientific research documents, whether they are published or not. The documents may come from teaching and research institutions in France or abroad, or from public or private research centers.

L'archive ouverte pluridisciplinaire **HAL**, est destinée au dépôt et à la diffusion de documents scientifiques de niveau recherche, publiés ou non, émanant des établissements d'enseignement et de recherche français ou étrangers, des laboratoires publics ou privés.

# Shattering and growth of cold clouds in galaxy clusters: the role of radiative cooling, magnetic fields, and thermal conduction

Fred Jennings,<sup>1,2★</sup> Ricarda S. Beckmann<sup>1</sup>,<sup>2</sup> Debora Sijacki<sup>2</sup> and Yohan Dubois<sup>3</sup>

<sup>1</sup>*Institute for Astronomy, University of Edinburgh, Royal Observatory, Blackford Hill, Edinburgh EH9 3HJ, UK*

<sup>2</sup>*Institute of Astronomy and Kavli Institute for Cosmology, University of Cambridge, Madingley Road, Cambridge CB3 0HA, UK*

<sup>3</sup>*Institut d'Astrophysique de Paris, UMR 7095, CNRS, UPMC Univ. Paris VI, 98 bis boulevard Arago, F-75014 Paris, France*

Accepted 2022 November 17. Received 2022 October 23; in original form 2022 July 14

## ABSTRACT

In galaxy clusters, the hot intracluster medium (ICM) can develop a striking multiphase structure around the brightest cluster galaxy. Much work has been done on understanding the origin of this central nebula, but less work has studied its eventual fate after the originally filamentary structure is broken into individual cold clumps. In this paper, we perform a suite of 30 (magneto)hydrodynamical simulations of kpc-scale cold clouds with typical parameters as found by galaxy cluster simulations, to understand whether clouds are mixed back into the hot ICM or can persist. We investigate the effects of radiative cooling, small-scale heating, magnetic fields, and (anisotropic) thermal conduction on the long-term evolution of clouds. We find that filament fragments cool on time-scales shorter than the crushing time-scale, fall out of pressure equilibrium with the hot medium, and shatter, forming smaller clumplets. These act as nucleation sites for further condensation, and mixing via Kelvin–Helmholtz instability, causing cold gas mass to double within 75 Myr. Cloud growth depends on density, as well as on local heating processes, which determine whether clouds undergo ablation- or shattering-driven evolution. Magnetic fields slow down but do not prevent cloud growth, with the evolution of both cold and warm phase sensitive to the field topology. Counterintuitively, anisotropic thermal conduction increases the cold gas growth rate compared to non-conductive clouds, leading to larger amounts of warm phase as well. We conclude that dense clumps on scales of 500 pc or more cannot be ignored when studying the long-term cooling flow evolution of galaxy clusters.

**Key words:** galaxies: clusters: intracluster medium.

## 1 INTRODUCTION

Galaxy clusters are the largest virialized structures in the Universe. Most of their baryon content ( $\geq 90$  per cent) can be found in the form of a hot intracluster medium (ICM) that fills the galaxy cluster and extends out to the virial radius (McNamara & Nulsen 2007; Kravtsov & Borgani 2012). The remaining baryons are bound in a collection of mostly early-type galaxies with old stellar populations, with the most massive brightest cluster galaxy (BCG) residing at their centre. The ICM is observed to possess a complex multiphase structure, with hot X-ray emitting gas ( $\geq 10^8$  K) coexisting with cold, dense structures ( $\leq 10^4$  K) that likely form via local thermal instabilities at radii of several tens of kpc from the cluster centre (McDonald, Veilleux & Mushotzky 2011; McCourt et al. 2012; Yang & Reynolds 2016; Beckmann et al. 2019; Das, Choudhury & Sharma 2021). This cold gas is found in and around the BCG, where it can be observed as visually spectacular H $\alpha$  emission nebulae that may fuel cold, clump accretion onto the BCG and their central supermassive black hole (SMBH; McDonald et al. 2010; Gaspari, Brighenti & Ruszkowski 2013; Tremblay et al. 2016, 2018). The most well-known example of this is the H $\alpha$  filaments in the Perseus cluster (Fabian 1994; Peterson & Fabian 2006; Fabian et al. 2008; McDonald et al. 2018), although filaments in many other clusters

have now been observed (e.g. Russell et al. 2017; Olivares et al. 2019; Jimenez-Gallardo et al. 2021; North et al. 2021). Cold molecular gas is also observed with radio observations of CO lines surrounding the BCG at radii of 50 kpc or so, as a result of inflows (Edge 2001; Salomé & Combes 2004; North et al. 2021), and most notably up to within 10 kpc of the central BCG with Atacama Large Millimeter/submillimeter Array (ALMA; McNamara et al. 2014; Russell et al. 2014; Fogarty et al. 2019). This inflow is thought to increase the growth efficiency and the magnitude of the feedback from the SMBH (DeGraf et al. 2017), with important implications for the morphology of the gas around the central object.

The existence of this cold gas reservoir is closely related to one of the major open problems in cluster physics today is the *cooling flow problem*. Naïve estimates of gas cooling in the ICM predict large-scale cooling flows, but assume an idealized, homogeneous cooling flow (Fabian 1994), assumptions that are quite untrue in the observed multiphase ICM, which has a much more complex substructure. The cooling flow model also neglects any heating processes that can inject thermal energy into the cold gas, for example through feedback processes. When comparing the cooling rate of hot gas via direct X-ray observations to the star formation rates in clusters, the discrepancy between the two suggests that there must in fact exist at least one non-gravitational source of thermal energy that offsets some of the cooling in these flows (e.g. Fabian 1994; Peterson et al. 2001, 2003; Hudson et al. 2010). This effect must be strong enough to suppress cooling rates by at least an order of magnitude.

\* E-mail: fred.jennings@ed.ac.uk

Understanding the lack of cold gas actually seen in clusters compared to estimates based on naïve cooling flow calculations is a crucial hurdle to be overcome by any complete model of galaxy cluster evolution. Much work on solving the cooling flow problem has been directed towards understanding this heating mechanism, and in particular towards understanding how energy injected by the central active galactic nucleus (AGN) powered by the SMBH in the BCG offsets radiative heating losses in the cluster over long periods of time (see e.g. Sijacki & Springel 2006; Vernaleo & Reynolds 2006; McNamara & Nulsen 2012; Gaspari et al. 2013; Gaspari 2015; Bourne, Sijacki & Puchwein 2019; Bourne & Sijacki 2021; Talbot, Sijacki & Bourne 2022). AGN feedback mainly operates in two modes: *kinetic*, which generates jets and bubbles; and a *radiative/quasar* mode in luminous AGN, where powerful winds may be driven by magnetic or radiation pressure, potentially displacing the cold gas. Feedback within galaxy clusters has been observed directly, as evidenced by jet-inflated bubbles with correspond to the so-called ‘X-ray cavities’, by e.g. Boehringer et al. (1993), Churazov et al. (2000), McNamara et al. (2000), Fabian et al. (2000), Birzan et al. (2004), Randall et al. (2011), Liu et al. (2020), and Ubertosi et al. (2021).

One crucial component of the overall cooling cycle of galaxy clusters is the evolution of cold gas once it has condensed from the hot phase. Large-scale cluster simulations have concluded that extended cold structures tend to fragment into smaller clumps over time (Gaspari et al. 2013; Li, Ruzsowski & Tremblay 2018; Beckmann et al. 2019), but lack the resolution to follow the evolution of individual small, cold clouds and ultimately to predict their fate. There are a wide range of potential scenarios for their evolution, with different consequences for large-scale cluster cooling flows. On one extreme, clouds could be quickly destroyed and mixed back locally into the hot phase. On the other extreme, small clumps could act as nucleation sites for cold gas condensation, which would make clouds grow in mass over time and eventually deliver large quantities of cold gas to the central BCG. If they survive for long periods of time, cold clouds could form part of a ‘fountain’ of cold gas in galaxy clusters; formed when the feedback from a central AGN breaks up inflowing filaments, they are accelerated in outflows and follow a ballistic trajectory only to slow down and eventually fall back towards the cluster centre, along with newly formed cold gas that has condensed via instabilities at radii of up to 50 kpc (McNamara & Nulsen 2007). Clouds that reach the BCG may be then accreted by its central SMBH and ultimately help to determine the behaviour of the very feedback that initially created them by increasing gas accretion rates and reorientation the spin axis of the AGN jet. Furthermore, cold clumps should be sufficiently destroyed by jets and/or mixed through further interaction with the ICM if feedback models are to successfully solve the cooling flow problem and explain the lack of cold gas in these systems. The simulations of Beckmann et al. (2019) show that a large fraction of cold gas originally in filaments can survive on small scales after interaction with the jets. Therefore understanding how cold clumps might survive or perish in the hot gas within an explicit clustercentric parameter space is key to the building of consistent models of both cluster cooling and heating, and of the coupling of feedback to the ICM.

Studying individual clouds embedded in a hot background medium that is moving at a relative velocity to the cloud is known as the *cloud-crushing problem* based on work by Klein, McKee & Colella (1994) who calculated the analytic time-scale on which small clumps get destroyed in such a scenario. Early simulations confirmed analytic expectations that clouds get disrupted and mix into the hot background medium (Klein et al. 1994; Cooper et al.

2009; Scannapieco & Brüggén 2015; Zhang et al. 2017). More recently, several authors have shown that in the presence of radiative cooling cold clouds can grow in some regions of the circumgalactic medium (CGM) parameter space (Armillotta, Fraternali & Marinacci 2016; McCourt et al. 2018; Sparre, Pfrommer & Vogelsberger 2019; Gronke & Oh 2020b; Kanjilal, Dutta & Sharma 2021) due to efficient mixing, but get still get destroyed if they are too small. At the surface between the hot and cold gas, a mixed warm phase forms due to the Kelvin–Helmholtz instability (Fielding et al. 2020). When the cooling times of this warm gas are sufficiently short in comparison to the cloud-crushing time, the cloud can grow over time (see Section 2 for details). Other non-thermal physics, such as magnetic fields and thermal conduction (Armillotta et al. 2016; Brüggén & Scannapieco 2016; Li et al. 2020; Sparre, Pfrommer & Ehlert 2020), can also influence the long-term mass evolution of cold clouds.

However, most of the work in the field has been conducted for a parameter space appropriate for the CGM and associated cold clouds, rather than the remnants of  $H\alpha$  filaments embedded in the ICM of a massive galaxy cluster. In this paper, we build on work in Beckmann et al. (2019), who demonstrated how cooling filaments in simulations are broken up into small (100 pc scale) clumps by interactions with the bimodal jets produced by a central SMBH. Being limited at a minimum resolution of 120 pc, this cluster-scale work was unable to follow the evolution of clouds on smaller scales. In this paper, we resimulate individual clouds with parameters typical to those seen in Beckmann et al. (2019) and the magnetized version of the same cluster (Beckmann et al. 2022a,b) to understand the long-term evolution of such dense gas fragments, including the impact of radiative cooling, small-scale cloud reheating, magnetic fields, and (anisotropic) thermal conduction.

This paper is structured as follows: in Section 2, we review the theory behind the cloud-crushing problem and present the set-up of our simulations in Section 3. The non-magnetized cloud-crushing problem is investigated in Section 4.1, with the impact of magnetic fields studied in Section 4.2, and that of thermal conduction in Section 4.3. Discussion and our conclusions are presented in Section 5.

## 2 THE CLOUD-CRUSHING PROBLEM

The classic set-up usually studied in the field is the *cloud-crushing problem*. This is an idealized set-up that studies how an individual cloud, embedded in a (usually) uniform background wind, evolves over time. The characteristic time-scale for the shredding of the cloud of uniform gas density  $\rho_{\text{cl}}$  and size  $r_{\text{cl}}$  within a uniform wind density  $\rho_{\text{wind}}$  and relative velocity of  $v_{\text{wind}}$  is the *cloud-crushing time-scale* (Klein et al. 1994),

$$t_{\text{cc}} \equiv \sqrt{\frac{\rho_{\text{cl}}}{\rho_{\text{wind}}} \frac{r_{\text{cl}}}{v_{\text{wind}}}} = \sqrt{\chi} t_{\text{cr}}, \quad (1)$$

over which Kelvin–Helmholtz instabilities and shocks will cross the cloud radius and shred the cloud material. The non-magnetized, non-radiative cloud-crushing problem is *scale-free* and can be entirely parametrized by the dimensionless density contrast  $\chi$  and the cloud-crossing time  $t_{\text{cr}}$ . The actual physical size, wind velocity, and cloud/wind densities can then be rescaled once these two parameters are determined. However, this approach breaks down in environments where radiative cooling in and around the cloud becomes important. This happens when the cooling time,

$$t_{\text{cool}} \equiv \frac{\rho \varepsilon}{\mathcal{L}} = \frac{3nk_{\text{B}}T}{2n_{\text{H}}^2 \Lambda(T, Z)}, \quad (2)$$

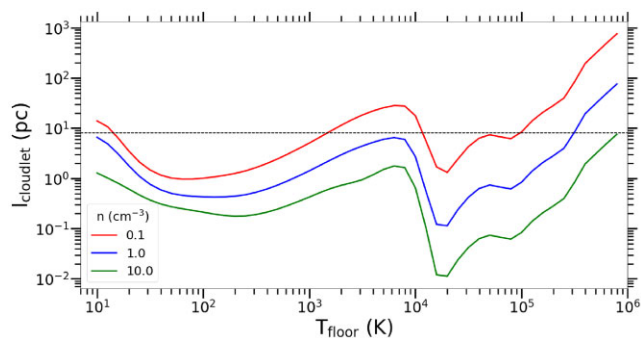


**Figure 1.** The minimum expected cloud size according to equation (4) as a function of the cold gas temperature for three different cloud number densities  $n$ . This plot assumes a metallicity of  $Z = 0.33 Z_{\odot}$ , with solar abundances of elements, and an adiabatic index of  $\gamma = 5/3$ . In general, denser clouds fragment to smaller clumps, but the evolution with temperature is not linear. The black horizontal line denotes our maximum spatial resolution of 8 pc adopted for our main production runs, but see Appendix B for higher resolution simulation results.

is comparable to or shorter than the cloud-crushing time. Here  $\Lambda(T, Z) \equiv \mathcal{L}/n_{\text{H}}^2$  is the *cooling function*,  $k_{\text{B}}$  is the Boltzmann constant,  $\varepsilon$  the specific energy,  $T$  the temperature,  $n$  the number density, and  $n_{\text{H}}$  is the hydrogen number density (Mo, van den Bosch & White 2010, chapter 8).

The ratio of cooling to cloud-crushing time-scales for clouds is

$$\theta \equiv \frac{t_{\text{cool}}}{t_{\text{cc}}} = \frac{3n_{\text{cl}}k_{\text{B}}T_{\text{cl}}v_{\text{wind}}}{2n_{\text{H,cl}}^2\Lambda(T, Z)r_{\text{cl}}\sqrt{\chi}}. \quad (3)$$

The cloud crushing is subdominant when the cloud is at much higher density than the wind (large  $\chi$ ), and when the cooling is efficient (i.e.  $\Lambda(T, Z)$  is large); for the metallicity of  $Z = 0.33 Z_{\odot}$  that we use (for both cloud and wind), the cooling function is strongly peaked between  $10^5$  and  $10^6$  K (Sutherland & Dopita 1993), meaning that the radiative losses should not be ignored, unlike studies of largely pristine environments such as the CGM where cooling may not be so important. This metallicity that we use is a well-known typical value for observations of the ICM, at least locally (see e.g. Mushotzky et al. 1978; Allen & Fabian 1998; Tozzi et al. 2003; De Grandi et al. 2004; Leccardi & Molendi 2008; Werner et al. 2013; Simionescu et al. 2015; Urban et al. 2017).

We can also equate the cooling and cloud-crossing time-scales to obtain a characteristic length at which the cloud should be able to respond dynamically to cooling-induced perturbations in the temperature and pressure (McCourt et al. 2018). This length  $l_{\text{cloudlet}} \sim c_s t_{\text{cool}}$  can be straightforwardly shown, for a fully ionized plasma with hydrogen fraction  $X$  (assuming an ideal gas speed of sound), to be equal to

$$l_{\text{cloudlet}} = \frac{3}{64} \left[ \frac{\gamma k_{\text{B}}^3 T_{\text{fl}}^3}{m_{\text{p}} X^4 n^2 \Lambda^2(T_{\text{fl}}, Z)} (3 + 5X - Z)^5 \right]^{1/2}, \quad (4)$$

where  $\gamma$  is the adiabatic index of the gas and  $T_{\text{fl}}$  is the temperature floor that the gas settles at, and  $m_{\text{p}}$  is the proton mass. The length scale on which clumps are dynamically responsive is inversely proportional to the number density and the value of the cooling function, and proportional to the temperature raised to the 3/2 power. We plot this length scale as a function of temperature in Fig. 1 for reference, using the cooling tables for dust-free, no cosmic rays, and no self-shielding model of Ploekinger & Schaye (2020), who have generated cooling rates using the spectral synthesis code CLOUDY (Ferland et al. 2017). Fig. 1 shows the analytical solution

for the minimum theoretical length scale (given by equation 4) that is expected in cloud shattering, if the cloud shatters continuously down to a floor temperature (given on the horizontal axis), and thus gives the rough size of the smallest clumps that should be seen in simulations, resolution permitting. Generally  $l_{\text{cloudlet}} < 1$  pc but very diffuse clouds in the temperature range  $10^3$ – $10^4$  K can have minimum sizes of 5 pc or more. The minimum cell length on our fine grid in the simulations presented in this paper is 8 pc for the majority of the runs, and we test a variety of temperature floor temperatures.

From the analytical result we see that we can expect to be able to only resolve clumps within a narrow range, which are around 0.5 orders of magnitude larger than our resolution length scale, although we get close to resolving the length floor over a broad range for diffuse clouds. We would expect further shattering beyond most of the smallest clumps produced in our simulation runs, and to gauge what effect this may have we perform a convergence test in Appendix B using a range of resolutions that are computationally feasible. We find that with increased resolution less cold gas forms initially (by up to 40 per cent for  $t < t_{\text{cc}}$ ), but at later times more cold gas forms due to the further shattering and higher mixing surface area-to-volume ratio. Therefore, we would expect that the our findings on the cold phase growth based on lower resolution simulation represent a conservative lower bound on the magnitude of this effect

### 3 NUMERICAL METHOD

#### 3.1 Nomenclature

Throughout this paper, we define a *cold phase* to include any gas at a temperature lower than the initial cloud temperature  $T < T_{\text{cl}}$ , a *warm phase* to include gas between the initial cloud and wind temperatures ( $T_{\text{cl}} < T < T_{\text{wind}}$ ), and a *hot phase* to include any gas at or above the initial wind temperature  $T \geq T_{\text{wind}}$ . For all quantitative measures of the three phases we see in the simulations, we use a straightforward temperature cut on the gas. For all simulations presented here,  $T_{\text{cl}} = 10^6$  K and  $T_{\text{wind}} = 10^8$  K. This wind/ICM temperature is consistent with X-ray observations of clusters (Reiprich & Böhringer 2002; Hudson et al. 2010; Frank et al. 2013) that measure X-ray temperatures mainly in the range 1–10 keV. The cloud temperature we use is consistent with the maximum temperature of so-called *dense gas* used to identify the clump objects generated within the cluster in Beckmann et al. (2019).

We also define as  $T_{\text{fl}}$  the minimum temperature to which gas is allowed to cool via radiative losses, the so-called cooling floor temperature. Furthermore we note another important temperature measure, the mixing temperature  $T_{\text{mix}} \simeq \sqrt{T_{\text{cl}}T_{\text{wind}}}$  given by Begelman & Fabian (1990), which is convenient for measuring some length scales of the problem (see Gronke & Oh 2020b).

#### 3.2 General set-up

The simulations presented in this paper were produced using the RAMSES code (Teyssier 2002), an adaptive mesh refinement magnetohydrodynamic (MHD) code. The simulations are conducted in 3D and include radiative cooling for all of our production runs, apart from a numerical experiment where we test the non-radiative set-up to highlight the differences. A subset of simulations also includes magnetic fields with different strengths and orientation, and (anisotropic) thermal conduction. To solve the MHD equations, RAMSES employs a second-order Godunov method (see Toro 2009), with a Monotonic Upstream-centered Scheme for Conservation Laws

**Table 1.** The parameters of the hydrodynamical runs, with the columns showing: (1) the run labels; (2) whether the run includes radiative cooling; (3) the initial cloud density  $\rho_{\text{cl}}$ ; (4) the initial wind (background ICM) density  $\rho_{\text{w}}$ ; (5) the length of the simulation box  $d_{\text{box}}$ ; (6) the size of the highest resolution element  $\Delta x$ ; (7) the value of the minimum temperature achieved through cooling  $T_{\text{fl}}$ ; and (8) the initial mass of the cold cloud. The crushing time-scale  $t_{\text{cc}}$  for all runs is 24.4 Myr, and the background wind velocity is 200 km s $^{-1}$  in all cases. All simulations have an initial background temperature of  $T_{\text{wind}} = 10^8$  K, and an initial cloud temperature of  $T_{\text{cl}} = 10^6$  K, except for HD0.1.1e4T0, which was initialized with  $T_{\text{cl}} = 10^4$  K.

Label	Cooling	$\rho_{\text{cl}}$ (H cm $^{-3}$ )	$\rho_{\text{w}}$ (H cm $^{-3}$ )	$d_{\text{box}}$ (kpc)	$\Delta x$ (pc)	$T_{\text{fl}}$ (K)	$M_0$ ( $M_{\odot}$ )
HD10.nc	$\times$	10	0.1	150	18	N/A	$1.28 \times 10^8$
HD0.1.nc	$\times$	0.1	0.001	150	18	N/A	$1.28 \times 10^6$
HD10	$\checkmark$	10	0.1	65	8	10	$1.28 \times 10^8$
HD1.0	$\checkmark$	1	0.01	65	8	10	$1.28 \times 10^7$
HD0.1	$\checkmark$	0.1	0.001	65	8	10	$1.28 \times 10^6$
HD0.1.1e4T0	$\checkmark$	0.1	0.001	65	8	10	$1.28 \times 10^6$
HD0.1.F5.5	$\checkmark$	0.1	0.001	65	8	$3 \times 10^5$	$1.28 \times 10^6$
HD0.1.F5.0	$\checkmark$	0.1	0.001	65	8	$1 \times 10^5$	$1.28 \times 10^6$
HD0.1.F4.5	$\checkmark$	0.1	0.001	65	8	$3 \times 10^4$	$1.28 \times 10^6$
HD0.1.F4.0	$\checkmark$	0.1	0.001	65	8	$1 \times 10^4$	$1.28 \times 10^6$
HD0.1.F3.5	$\checkmark$	0.1	0.001	65	8	$3 \times 10^3$	$1.28 \times 10^6$
HD0.1.F3.0	$\checkmark$	0.1	0.001	65	8	$1 \times 10^3$	$1.28 \times 10^6$

(MUSCL)–Hancock scheme to solve the Euler equations and compute fluxes across cells. RAMSES uses an octree refinement method to adaptively refine the space, and models magnetic fields as face-centred quantities with constrained transport to satisfy the solenoidal constraint  $\nabla \cdot \mathbf{B} = 0$  (Fromang, Hennebelle & Teyssier 2006). A Harten–Lax–van Leer contact (HLLC) Riemann solver (Toro 2009) was used for simulations without magnetic fields, with a Harten–Lax–van Leer discontinuities (HLLD) solver (Miyoshi & Kusano 2008) used for later MHD runs. The Courant factor was set to 0.8 for adaptive time-stepping, for which RAMSES uses a second-order mid-point scheme. We use the YT PROJECT PYTHON package (Turk et al. 2010) for all analysis.

### 3.3 Initial conditions and refinement

All simulations presented in this paper have a similar set-up: a spherical cold cloud of radius  $r_{\text{cloud}} = 500$  pc and temperature  $T_{\text{cl}} = 10^6$  K is placed in a uniform hot background medium of temperature  $T_{\text{wind}} = 10^8$  K. We fix the initial cloud density contrast to  $\chi = \rho_{\text{cl}}/\rho_{\text{w}} = 100$ , but vary both the initial cloud density  $\rho_{\text{cl}}$  and the initial wind density  $\rho_{\text{w}}$  (see Table 1 for details). This cloud temperature was selected in order to initialize the clouds in pressure equilibrium with the surrounding hot medium, whose temperature is typical for the ICM of galaxy clusters. This overdensity was chosen as the typical overdensities in the simulations of Beckmann et al. (2019) range from around 2 to 4 (see their fig. 4). We select the lowest value in this range because this corresponds to the smallest crushing time-scale, meaning we can simulate longer into the dynamical lifetime of the cloud.

Simulations are conducted in the frame of the cold cloud, which is initialized with zero bulk velocity. Instead, the background medium is given a bulk velocity of 200 km s $^{-1}$ , in line with observations of line-of-sight velocities in cluster centres (Salomé et al. 2006; McDonald, Veilleux & Rupke 2012; Tremblay et al. 2016; Olivares et al. 2019), and corresponding to the peak of the velocity distribution of the clumps produced in Beckmann et al. (2019) (see fig. 7 of that work). This is equivalent to a cloud Mach number of  $\mathcal{M} = 2$ . A random velocity dispersion field of normal distribution centred around zero and with standard deviation of 50 km s $^{-1}$  within the hot medium and 30 km s $^{-1}$  within the cloud

was added to the cloud and wind bulk velocities in order to avoid grid-locking effects and roughly model the turbulence that may play an important role in galaxy clusters (e.g. Schuecker et al. 2004; Churazov et al. 2012; Gaspari & Churazov 2013; Walker, Sanders & Fabian 2015; Hofmann et al. 2016; Hitomi Collaboration et al. 2018; ZuHone et al. 2018). We calibrated the mean and variance of the velocity dispersion to values found in and around clumps produced by the simulations presented in Beckmann et al. (2019). No further turbulence driving is added throughout the simulation.

The simulation is initialized with a passive scalar, initially set to unity within the cloud and zero outside, which is advected with the flow throughout the simulation. This scalar is used both during the simulation run and in post-processing to help distinguish mixed material from pristine background gas, as cells with high  $f_{\text{scalar}} = \rho_{\text{scalar}}/\rho_{\text{gas}}$  are dominated by gas originally found in the cloud, while those with low  $f_{\text{scalar}}$  are dominated by gas initially found in the hot background medium. Note however that quantitative measures of masses for the three fluid phases that we will discuss later on, use only a cut on the temperature of the plasma, as discussed above.

At the start of our simulations the cloud is set up to be in pressure equilibrium with the ICM in all runs, as this is appropriate in a galaxy cluster environment. All simulations were initiated with a metallicity of  $Z = 0.33 Z_{\odot}$ , as is typical for clusters (Baumgartner et al. 2005; Lovisari & Reiprich 2019), and this metallicity was kept constant throughout. The metallicity of the cloud is not expected to deviate significantly from the background medium, since clouds originally likely condense from the hot ICM. In practice, a metallicity gradient within the cluster and star formation occurring in and around cold clumps may lead to a range of different metallicity values for dense clumps, but note that the observed metallicity gradients of the ICM are typically shallow (Leccardi & Molendi 2008).

No gravity is included in our simulations. The free-fall time of our clouds is  $t_{\text{ff}} = \sqrt{3\pi/32G\rho_{\text{cl}}}$  that, for our fiducial run (the lowest density we test), means the free-fall time is approximately 150 Myr that corresponds to around  $6 t_{\text{cc}}$ . As  $t_{\text{cool}} < t_{\text{cc}}$  in all of our radiative set-ups, there is a pressure-driven collapse on subcrushing time-scales during which gravity is subdominant and therefore not included explicitly here.

In MHD simulations, the magnetic field was initialized as a uniform field that is either initially parallel (‘aligned’) or perpen-

**Table 2.** The parameters of MHD runs, with columns showing: (1) the names; (2) the magnetic field strength  $B_0$ ; (3) the initial orientation of the magnetic field relative to the initial bulk flow velocity (either normal to the flow or aligned with the flow); and (4) the type of thermal conduction type (if at all). All runs are variations of HD10 and share its parameters where not explicitly stated otherwise.

Name	$B_0$ ( $\mu\text{G}$ )	Orientation	Conduction
MHD_1N	1.0	Normal	✗
MHD_1A	1.0	Aligned	✗
MHD_3N	3.0	Normal	✗
MHD_3A	3.0	Aligned	✗
MHD_5N	5.0	Normal	✗
MHD_5A	5.0	Aligned	✗
MHD_1N_i	1.0	Normal	Isotropic
MHD_1A_i	1.0	Aligned	Isotropic
MHD_3N_i	3.0	Normal	Isotropic
MHD_3A_i	3.0	Aligned	Isotropic
MHD_5N_i	5.0	Normal	Isotropic
MHD_5A_i	5.0	Aligned	Isotropic
MHD_1N_a	1.0	Normal	Anisotropic
MHD_1A_a	1.0	Aligned	Anisotropic
MHD_3N_a	3.0	Normal	Anisotropic
MHD_3A_a	3.0	Aligned	Anisotropic
MHD_5N_a	5.0	Normal	Anisotropic
MHD_5A_a	5.0	Aligned	Anisotropic

dicular (‘normal’) to the flow. Thermal conduction is modelled following Dubois & Commerçon (2016), with a thermal conduction coefficient equal to  $\kappa_{\text{Spitzer}} = n_e k_B D_C$  (Spitzer 1962), where  $n_e$  is the electron number density,  $k_B$  is the Boltzmann constant,  $D_C = 8 \times 10^{30} \left(\frac{k_B T_e}{10^8 \text{ K}}\right)^{\frac{5}{2}} \left(\frac{n_e}{10^{-2} \text{ cm}^{-3}}\right)^{-1} \text{ cm}^2 \text{ s}^{-1}$  the thermal diffusivity, and  $T_e$  the electron temperature. In the case of anisotropic thermal conduction, the perpendicular conductivity is set to  $\kappa_{\text{perp}} = 0.0001 \kappa_{\text{Spitzer}}$ .

The size of the simulation box is chosen such that the flow crossing time at the wind velocity is several tens of crushing times. In practice we never simulate for this long, and all runs are stopped before the mixed tail of the cloud reaches the edge of the simulation domain, so no material is lost from the simulation. Most simulations were performed in a box size of 65 kpc, with a root grid of  $32^3$  (refinement level 5) cells that was adaptively refined by eight more levels up to a maximum resolution of  $\Delta x = 8$  pc. The initial conditions are refined using concentric spheres centred on the cloud, with the highest refinement level incorporating the entire initial cloud. Refinement then proceeds adaptively where a cell is refined at the highest level of refinement if  $f_{\text{scalar}} > 10^{-6}$ , and progressively derefined otherwise.

All simulation parameters are summarized in Table 1 for the hydrodynamical runs and in Table 2 for MHD simulations with and without conduction.

### 3.4 Cooling

Radiative cooling in RAMSES is computed using values given in the cooling tables of Sutherland & Dopita (1993) above  $10^4$  K and those from Rosen & Bregman (1995) for temperatures below. In our simulations, gas cools to a minimum fiducial temperature of  $T_{\text{fl}} = 10$  K (although we do run a suite of tests investigating the effect of changing this value in Section 4.1.3).

In galaxy clusters, both cloud dynamical and cloud-crushing time-scales for cold clouds are comparable to or longer than the cooling time of the hot ICM. However, observationally, the ICM temperature does not change significantly over sufficiently long time-scales, as the bulk of cooling of the ICM in galaxy clusters

is offset by various heating sources, from energy injected by the AGN to possibly thermal conduction. To mimic the impact of such background heating in the simulations presented here, radiative cooling is only permitted in gas above a minimum concentration of a passive scalar originally only placed in the cold cloud (see Section 3.3). This approach prevents the catastrophic cooling of the hot ICM background gas (as opposed to clump gas and mixed gas, which we allow to cool freely) that would otherwise occur over time-scales that are short compared to the dynamical time-scale, at variance with observations. We set the required passive scalar value to  $f_{\text{scalar}} > 0.001$ , and still permit hot gas to cool via in-cell mixing with colder fluid. In MHD simulations, spurious magnetic heating occurred in a very small number of cells in and around the clouds. To prevent such ‘hotspots’ from occurring and from slowing the simulation, we enforced a minimum density floor of  $0.0005 \text{ cm}^{-3}$ . Convergence tests showed no statistically significant impact on the long-term evolution of simulations from such a density floor.

### 3.5 Clump finding

To gather statistics on the distribution of individual clumps in our simulations, we use the water-shed segmentation-based structure finding algorithm PHEW (Bleuler et al. 2015). Clumps are identified in all gas with  $T < 3 \times 10^7$  K, and densities above  $n > 0.02 \text{ cm}^{-3}$ . All clumps with a relevance (peak-to-saddle ratio) of less than 30 are merged through the saddle into the neighbouring clump.

## 4 RESULTS

### 4.1 Radiative cooling and cloud growth

In this section, we study the impact of varying cloud and background gas parameters to understand how local gas properties impact the evolution of cold clumps in galaxy clusters. All simulations presented here have no magnetic fields, while the simulations with magnetic fields are discussed in Section 4.2. Specific simulation parameters are outlined in Table 1.

#### 4.1.1 The impact of radiative cooling

Two runs were performed with cooling turned off in order to quantify the impact of cooling and compare our work against the large existing body of work that does not consider cooling.

The cloud-crushing time-scale for the clouds we use is 24.4 Myr, and the cooling time-scale is initially a factor  $10^{4.6}$  shorter than this for the densest cloud HD\_10, and  $10^{3.6}$  and  $10^{2.6}$  times shorter than the crushing time for HD\_1.0 and HD\_0.1, respectively. As shown in Fig. 2, cooling completely changes the morphology of cold clouds. Without cooling (left-hand panel), cloud gas is mixed rapidly into the hot phase, while with cooling (right-hand panel) the cold cloud is shattered into many small fragments that persist. More quantitatively, Fig. 3 shows that the clump in the HD0.1\_nc run loses 70 per cent of its initial mass by  $t = 2 t_{\text{cc}}$ , which rises to 99 per cent by  $t = 3 t_{\text{cc}}$ . The cloud being destroyed on a time-scale of the order of  $t_{\text{cc}}$  is in agreement with standard results of the cloud-crushing problem. This evolution is independent of the initial clump density that we vary by two orders of magnitude (compare the low-density non-cooling cloud HD0.1\_nc to the high-density non-cooling cloud HD10\_nc in Fig. 3).

When radiative cooling is included, the cloud follows a completely different evolution, as shown in Figs 3 and 4, which quantify the time

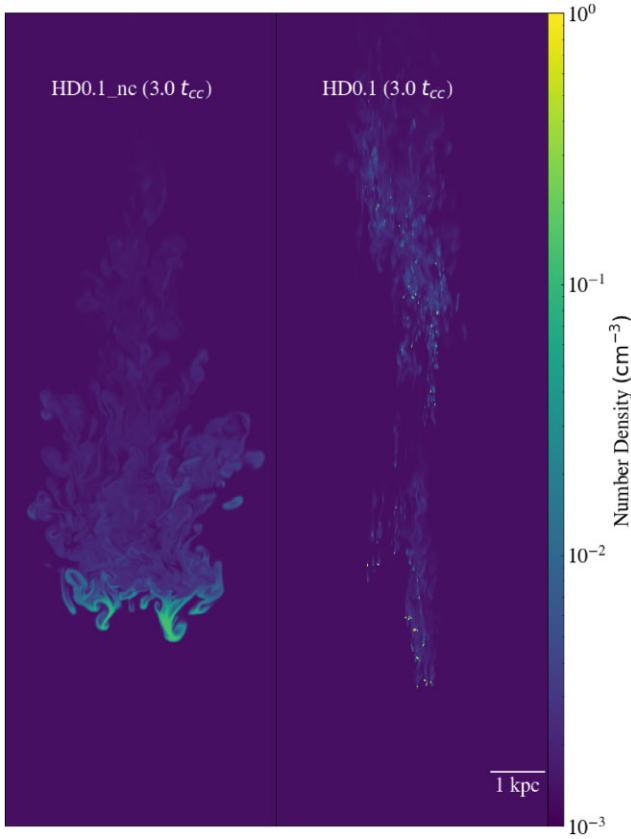


**Figure 2.** Number density slices showing the difference in evolution after three cloud-crushing times between the run without cooling (HD0.1\_nc, left) and an identical cloud run with cooling (HD0.1, right). Radiative cooling promotes shattering of the cloud during the early evolution, with cloud morphology being distinctly different.

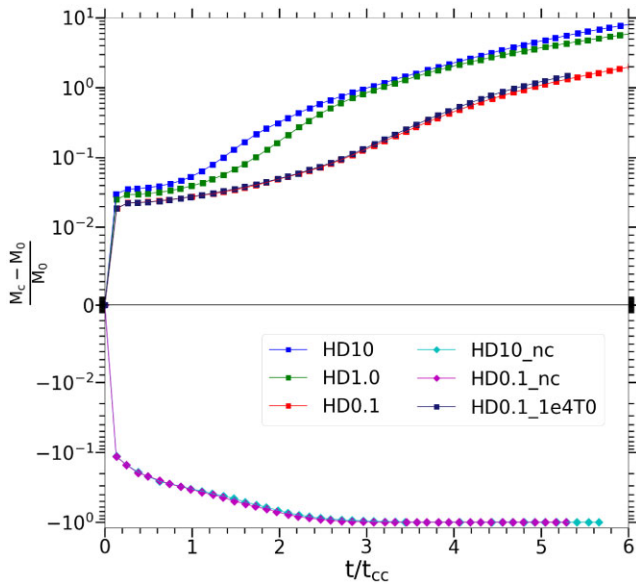


**Figure 3.** The fractional change in cold gas mass shown for cooling and non-cooling simulations at different cloud densities. The cloud is destroyed within a few  $t_{cc}$  if cooling is not present consistent with a large body of previous literature. However, in radiative simulations significant cloud mass growth is seen for all densities explored.

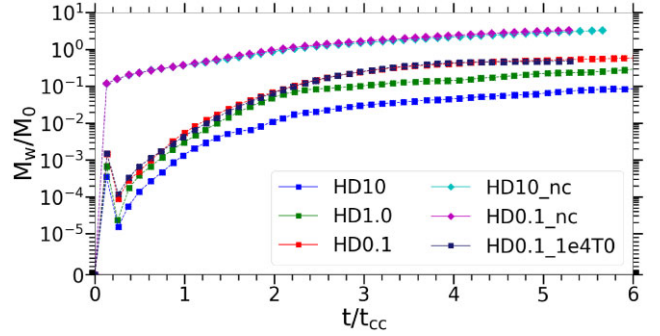


**Figure 4.** Time evolution of the warm gas fraction normalized to the original cloud mass for different initial densities. In the presence of radiative cooling, the amount of warm gas is reduced in comparison to the non-cooling runs as the warm gas is depleted by gas cooling into the cold, dense phase. However, warm gas gradually builds up over time, with initially more diffuse clouds producing a larger fraction of warm gas.

evolution of the cloud and wind mass, respectively, and visualized in Fig. 5 that illustrates the time evolution of the projected number density. Most notably, rather than being destroyed, the total mass of the cloud grows significantly over time. This long-term cloud growth is expected from previous work by Li et al. (2020) and Gronke & Oh (2020b), who both predict a minimum cloud survival radius (of 6.5 and 3.3 pc, respectively, computed using equations 3 and 5 from Kanjilal et al. 2021) well below the initial 500 pc radius of the cloud studied here.

Initially, for  $t \lesssim t_{cc}$  the cold mass in the clouds grows slowly, but then it accelerates, doubling within  $5 t_{cc}$  even for the lowest initial cloud density explored (see Fig. 3). This cold mass growth is more pronounced for the runs with higher initial cloud densities (see Section 4.1.2 for a more detailed discussion) and for simulations performed at higher resolution (see Appendix B).

In Fig. 6, we investigate whether this increased growth is due to a larger number of individual clumps, or an increased mass per clump. To do so, we identify individual cloudlets in the wake as described in Section 3.5 and then study the statistics of this ensemble of cloudlets for each simulation over time. As can be seen in Fig. 6, the total growth in cloud mass is both due to a higher number of individual clumps, and due to a higher mass per clump.

The process commences with an initial collapse phase, during which the cloud cools rapidly and compacts on subcrushing time-scales. Density inhomogeneities are seeded in the collapse, and material starts to ablate from the main cloud in the form of individual fragments with radii in the range 5–100 pc, as shown in Fig. 6. Over time, the original cloud is entirely broken up and the resulting clumps, as well as the warm, diffuse material between them, form an extended clumpy wake, as shown in Fig. 2 and the late-time panels of Fig. 5. The typical slope of  $dN_{clumps}/dM$  is of the order of  $-0.7$  (see fitted slopes in Fig. 6), which is somewhat shallower than the  $-1$  measured in Gronke et al. (2022), which suggests that the higher levels of turbulence in Gronke et al. (2022) accelerate shattering. We find, by analysing the typical range of clump sizes and densities seen post-shattering, that the characteristic crushing time-scale of the clumps is roughly the same as that of the initial parent cloud, allowing us to continue use of  $t_{cc}$  as a robust characteristic time even after the shattering process. The overdensity  $\chi$  does however increase, to approximately  $100 \times T_{cl,0}/T_{cl,ps}$  for our initial overdensity of 100 and a post-shattering temperature  $T_{cl,ps}$  when the cloud attains approximate hydrostatic equilibrium again.

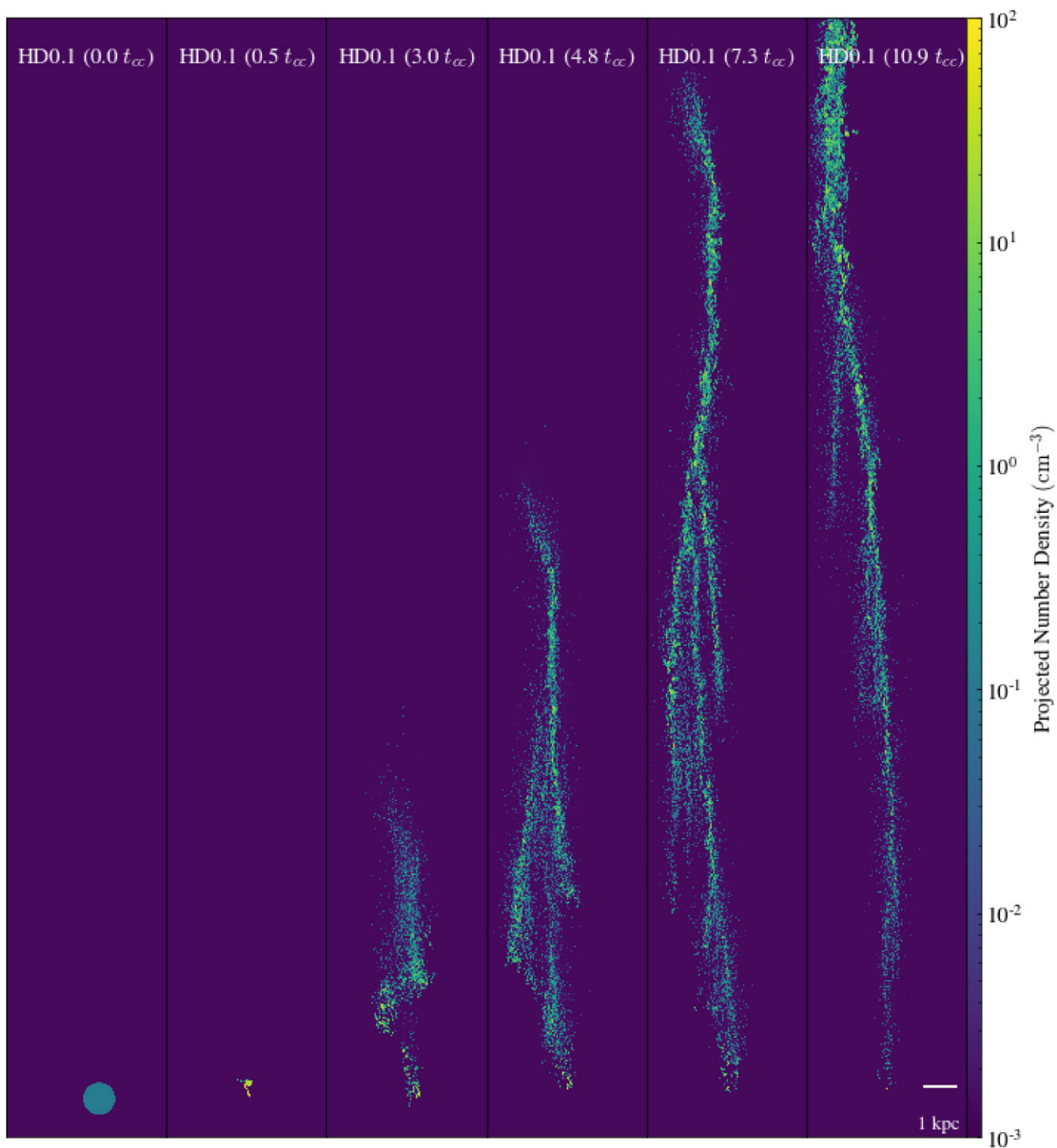


**Figure 5.** Density-weighted projections of the number density  $n$  shown at different times for simulation HD0.1. The cloud collapses and fragments within one crushing time-scale, and the resulting clumpets then interact dynamically with the wind, forming an extended tail. Note that each projection is centred on the most upstream clump material.

We run one cloud in initial hydrostatic non-equilibrium, HD0.1-1e4T0, by setting the initial cloud temperature to  $T_{cl} = 10^4$  K, to examine how sensitive the shattering and further evolution is to the initial temperature and pressure of the clump. As can be seen in the mass evolution plots of Figs 3 and 4, shattering occurs quickly enough that evolution is insensitive to the initial cloud temperature, and the only cloud property we find to be important is the density.

The late-time evolution after several crushing times is driven by the evolution of the wake in the cooling case. The mixing of the cold fragments with the hot ICM generates a warm, mixed phase, which makes up the wake of the clump, and trails any high-density remnants of the original clump that remain at the ‘head’ of the cloud. The amount of gas contained in this wake grows over time but remains small in comparison to the cold gas mass, reaching about 25 per cent

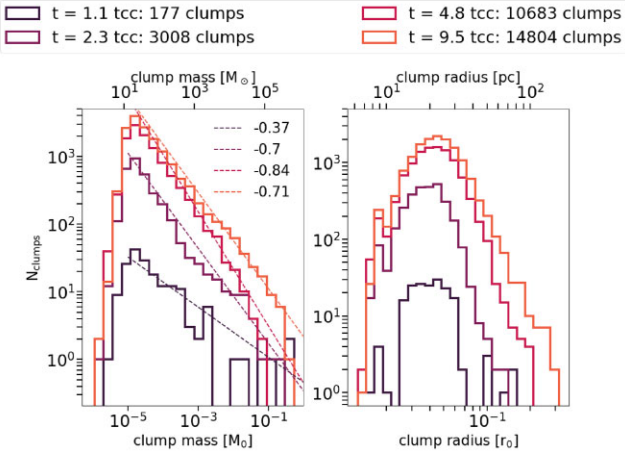


**Figure 6.** Distribution of clump masses (left) and clump radii assuming spherical clumps (right) for simulation HD0.1 at four different epochs. Insets in the left-hand panel show the slopes of the power-law fit for clump masses above  $10^{-5} M_{\odot}$ .

of the original cloud mass by  $t = 3 t_{cc}$  for HD0.1 (see Fig. 4). This warm gas has a very short cooling time, as can be seen in Fig. 7, due to a peak in the cooling function  $\Lambda(T)$  between  $10^5$  and  $10^6$  K. In the most extreme cases, the cooling time can be 5–6 orders of magnitude shorter than the crushing time-scale. For such a short cooling time, cooling dominates the evolution of the gas, and gas transfers quickly through the temperature–density phase space from high temperature, diffuse to cold, newly condensed cloud.<sup>1</sup> The mixed phase condenses onto the clump as *new* cold gas, which means that the cold fragments act as nucleation sites for cold condensate within the hot ICM. We find that this is dominant over mixing losses, resulting in the growth of the total cold gas mass over time (see Fig. 3). The no-cooling cases, display no such growth, even though a significant amount of warm gas is produced, with the fraction of warm gas more than an order of magnitude larger in the no-cooling runs in comparison to the initial cloud mass (see Fig. 4). This markedly different evolution with cooling shows the importance of including radiative cooling in driving the evolution of cold clouds in hot atmospheres of galaxy clusters.

Qualitatively, our results on cold cloud growth agree with recent results by Gronke & Oh (2020b), Li et al. (2020), and Jennings & Li (2021), as well as with results by Gronke & Oh (2018) even though the latter do not see the same amount of shattering as they impose a higher temperature floor of  $4 \times 10^4$  K (see Section 4.1.3 for a discussion on the impact of cooling floors). The cold clumps simulated here exceed the pressure condition required for shattering put forth by Gronke & Oh (2020b), namely  $P_{cl,ps}/P_{cl,0} \sim T_{cl,ps}/T_{cl,0} \lesssim 0.33$ , where  $T_{cl,ps}$  is the post-shattering cloud temperature, equal to the cooling floor temperature. We do not find any significant post-shattering coagulation of fragment clumps, probably due to the extreme pressures generated by the large temperature gradients, with the fragments being well separated after the post-shattering expansion. This can be clearly seen at late times in Fig. 5.

<sup>1</sup>We note that the bimodal feature in the temperature range  $10^4$ – $10^6$  K in Fig. 7 is due to the structure of the flow, and results from a combination of cooling and mixing at the surface of individual cold clumps. The left-hand feature is formed by gas upstream of individual clumps, and consists predominantly of gas that originates in the hot wind. The right-hand feature is composed of gas downstream of individual clumps, which contains a higher percentage of gas ablated from the clumps and is therefore at higher density.

The final size of clumpets needs to be considered in this context too. McCourt et al. (2018) put forth an argument that clouds will shatter until their clumps are small enough that the sound-crossing time is of order the cooling time, and thus cooling can occur isobarically. This occurs when clumps reach a physical length scale of  $l \sim c_s t_{cool}$ , which occurs approximately on the time-scale of  $t_{cool}$ . McCourt et al. (2018) show that clouds should shatter down to a size of  $l_{cloudlet} \sim c_s t_{cool} \sim (0.1 \text{ pc})/n$ , and this has been further confirmed by other simulation works (see e.g. Gronke & Oh 2020b). The largest characteristic length of these cloudlets in our simulations is expected to be around a parsec, an order of magnitude smaller than our minimum resolved scale, even with the high resolution we have adopted. Ideally, a resolution two order of magnitude better than our simulation runs should be used, to investigate whether shattering stops at this characteristic scale, or if clumps will fragment even more, but this is computationally unfeasible with our current set-up since  $r_{cl}/l_{cloudlet} \gg 1$ .

In summary, we reproduce the destruction or growth of the cloud on crushing time-scales found by similar studies. For the parameter space of cold clouds in a hot cluster environment, we find that clouds grow in mass on time-scales relevant for their trajectories when radiative cooling is taken into account. This growth is significant, and leads to cold clouds acting as nucleation sites within the hot ICM, with condensation beginning after only a few crushing time-scales, which in cluster environments translates to a few tens of Myr.

#### 4.1.2 Density dependence

We now compare the effects of altering the initial cloud density on the evolution of clouds themselves, by comparing runs with initial cloud densities of  $\rho_{cl} = 10 \text{ cm}^{-3}$  (HD1.0) and  $\rho_{cl} = 1 \text{ cm}^{-3}$  (HD1.0) to the fiducial run HD0.1 that has cloud density  $\rho_{cl} = 0.1 \text{ cm}^{-3}$ . All three simulations have the same overdensity  $\chi = \rho_{cl}/\rho_w = 100$ , and are therefore identical within the context of scale-free considerations.

As expected from analytic work, the absolute density of the cloud does not change the mass evolution in the absence of cooling as long as  $\chi$  is constant. This can be clearly seen by the identical time evolution of both the warm and cold gas for simulations HD1.0\_nc and HD0.1\_nc in Figs 3 and 4.

It is only with the addition of cooling that the absolute density of the cloud makes a difference to its evolution. An initially lower density cloud forms lower density fragments post-shattering as would be expected, and the lower density of the clumpets in the wind results in greater mixing of cold gas into a warm phase. This can be clearly seen in Fig. 4 by the larger amount of warm gas generated by the lower density cloud, in comparison to its initial mass. This confirms that the presence of cooling breaks the scale-free nature of the problem, by introducing an additional characteristic time-scale that depends on both the cloud density and temperature (as well as metallicity, but this is kept constant in our runs). As the cooling time is shorter for denser material, initially denser clouds show faster mass growth due to the more rapid condensation of gas from the warm to the cold phase. The impact of the higher density mixed gas on the cooling time for all three simulations can be seen in Fig. 7, with the fastest cooling regime in the warm phase only occupied by the densest clouds. Interestingly, all three simulations reach a rough equilibrium between mixing new gas into the warm phase, and cold gas condensing into the cold phase, but the equilibrium amount of warm gas is lower for initially higher density clouds (see Fig. 4).

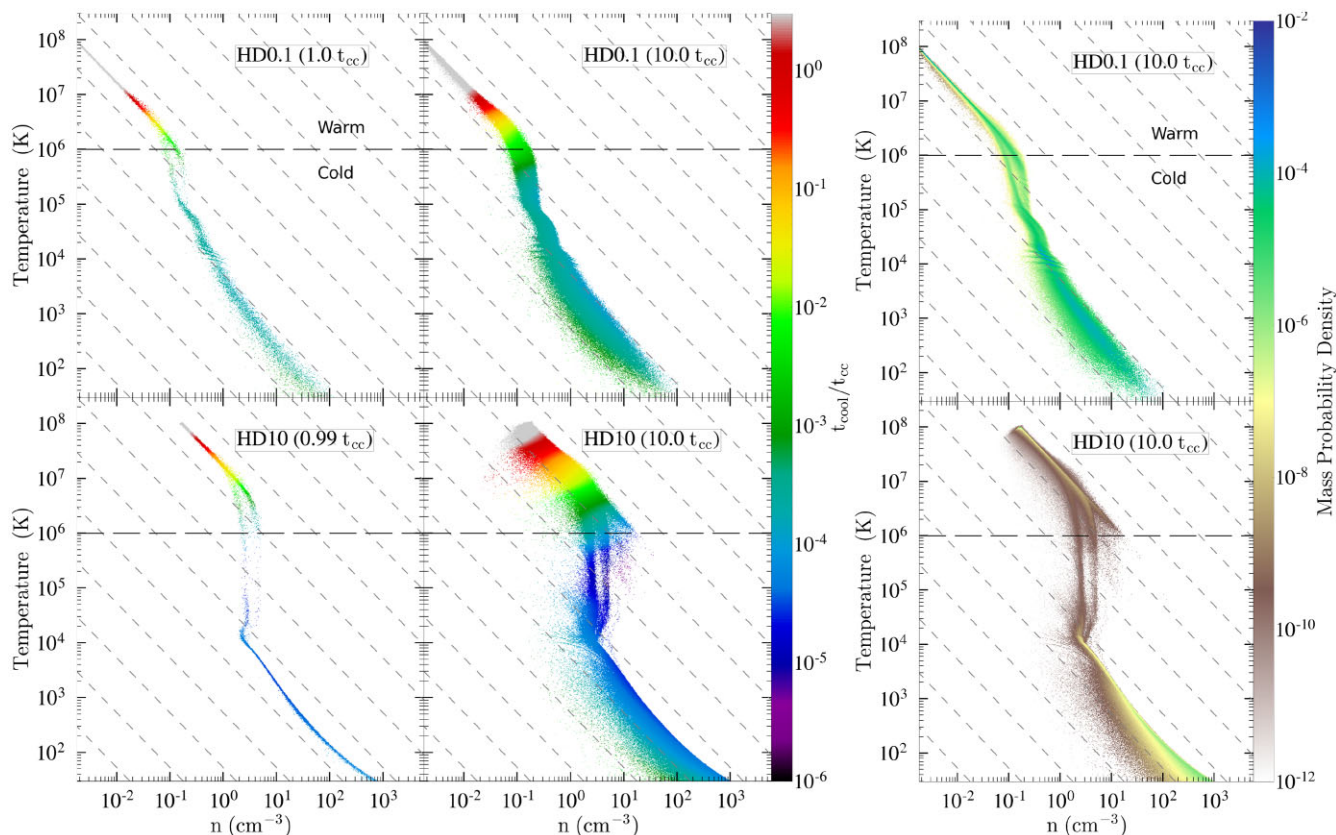


**Figure 7.** Left: binned temperature–density phase space occupied by the clouds for simulations HD0.1, and HD10, with the colour map showing the ratio of cooling time to crushing time  $\theta$  at three different times (left to right). We also show the regions we define throughout the paper as ‘warm’ gas ( $10^6 < T < 10^8$  K) and ‘cold’ gas ( $T < 10^6$  K). The change in initial cloud density (as well as wind density) leads to a different phase-space region of the cooling function being sampled by the cloud, particularly in the warm phase; at higher densities the cooling times are much shorter, and cooling can take place as much as nearly six orders of magnitude faster than cloud crushing for the densest cloud we test. The densest cloud HD10 cools isochorically in the warm phase by approximately one and a half orders of magnitude more than the least dense cloud, and settles later onto the isotherm that will take the temperature down to  $T_{\text{fl}}$ . Right: we instead show the mass probability density of the two clouds each after  $10 t_{\text{cc}}$ . Though the initial overdensities were identical, the more dense cloud HD10 holds more of its mass in dense, cold fluid, and has a more bimodal distribution between the cold and hot phase, whereas HD0.1 has a mass distribution more evenly distributed through the warm phase as well.

For our densest cloud modelled here, HD10\_nc, the initial cloud conditions are such that Li et al. (2020) predict that clouds with an initial radius of  $r_{\text{cl,init}} < 651$  pc (computed using equation 5 in Kanjilal et al. 2021) should not survive, which is larger than our initial cloud radius of 500 pc. By contrast, Gronke & Oh (2020b) predict a minimum cloud survival radius of 334 pc (computed using equation 3 in Kanjilal et al. 2021), and therefore predict cloud HD10\_nc should survive. With only a single cloud in this borderline region between the two regimes, we refrain from strong statements about either criterion. Instead, we simply note that HD10\_nc exhibits robust growth in our simulations and that this range of radii would be an interesting range to probe in future work.

We conclude that cooling is the dominant mechanism determining the evolution of the cloud for all clouds within the two orders of magnitude in density probed here. We also confirm that in cluster environments, where cooling dominates the evolution of cold clouds, scale-free studies are insufficient and the parameter space needs to be explored widely. The smaller the ratio of cooling time to cloud-crushing time  $\theta$  (see equation 3), the faster cold clumps in the ICM can condense new gas and grow, with all cases tested here more than doubling the clouds initial mass on time-scales of around 150 Myr, and some increasing it by almost a factor of 10.

#### 4.1.3 Cloud crushing and small-scale heating

The sub-kpc scale physics that takes place in cold clouds within galaxy clusters is poorly understood. However, observations show the presence of warm gas, despite short cooling times, which suggests that clouds need to be persistently powered. Over the years, many processes have been suggested as the source of this heating, from photoionization by the central AGN (e.g. Heckman et al. 1989; McNamara & Nulsen 2012) or massive stars (Canning et al. 2014), via thermal conduction (Voit et al. 2008) and magnetic reconnection (Hanasz & Lesch 1998; Tanuma et al. 2003; Churazov, Ruszkowski & Schekochihin 2013) to cosmic ray streaming heating (Ruszkowski, Yang & Reynolds 2018), to name a few. Stars can form in ‘knots’ along filaments (Vantyghem et al. 2018), and these sites may also provide some heating and feedback to the cold gas once fragmented. So far, no consensus has been reached on the origin of cloud heating, but such energy injections at the cloud radius would off-set some of the cooling and prevent clouds cooling below an effective temperature floor. This floor would of course be expected to be time varying, with the characteristic time-scale of the most dominant heating mechanism setting the time-scale of variation. However, without knowing where the dominant energy input comes from, we choose to keep the floor constant throughout our simulations.

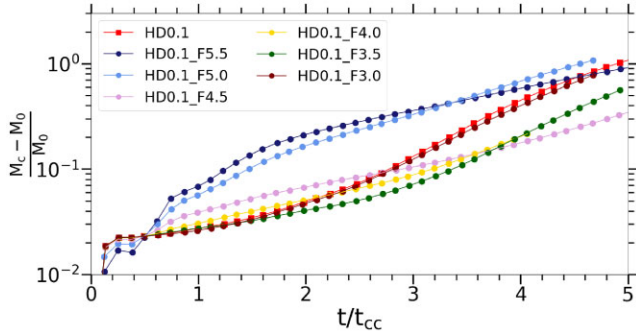


**Figure 8.** The normalized cold gas mass fraction for variations of HD0.1 run with different cooling floor temperatures  $T_{\text{ff}}$ . They are compared to our flagship run HD0.1, which has an effective temperature floor of  $T_{\text{ff}} = 10$  K. Trends are non-linear, with cold gas mass growth the fastest for both high ( $T_{\text{ff}} \geq 10^5$  K) and low ( $T_{\text{ff}} \leq 10^3$  K) cooling floors, but suppressed for  $10^3 < T_{\text{ff}} < 10^5$  K.

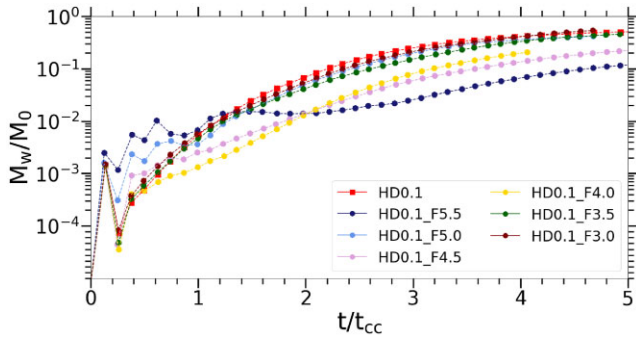


**Figure 9.** The normalized warm gas mass fraction for each variant of HD0.1 run with different cooling floor temperatures  $T_{\text{ff}}$ . Lower cooling floors produce more warm mass in the temperature range  $10^3 \leq T_{\text{ff}} < 10^{5.5}$  K, but significantly lower cooling floors again reduce the warm gas mass.

In the simulations presented here, we test the impact of such small-scale heating and feedback processes, as well as the heating effects of a radiation background within the cluster, by varying the cooling floor, i.e. the minimum temperature that gas can reach through radiative cooling. The implicit assumption is that at this temperature, the energy losses from radiative cooling match the combined heating effects of the processes we do not explicitly model. To test the robustness of our general results against this choice of cooling floor, we select one simulation (HD0.1) to be repeated with a variety of cooling floor temperatures  $T_{\text{ff}}$ . These runs are detailed in Table 1.

We find that clouds grow for all choices of cooling floor tested here. During the initial cloud disruption phase ( $t < 0.5 t_{\text{cc}}$ ), a higher cooling floor produces less cold gas (Fig. 8) and more warm gas (Fig. 9). The cloud with a cooling floor at  $3 \times 10^5$  K hardly shrinks in radius during  $t < t_{\text{cc}}$ , as the initial cooling and resulting loss of pressure is strongly reduced, while clouds with lower cooling floors contract significantly as can be seen in the images in Fig. 5 for our fiducial HD0.1 run.

Beyond  $1 t_{\text{cc}}$ , the evolution becomes more complex. There is a general trend for higher cooling floors to produce more cold gas for  $0.5 t_{\text{cc}} < t < 4 t_{\text{cc}}$ , while for lower cooling floors the cold gas mass increase is lower initially but then accelerates after several crushing times. The lower the cooling floor, the faster the turn-up occurs,

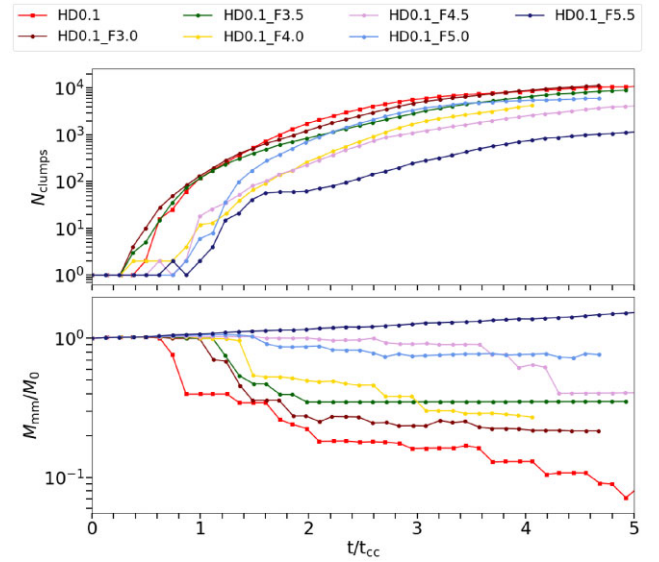


**Figure 10.** Time evolution of the number of clumps (top panel) and the mass of the most massive clump as a function of initial cloud mass (bottom panel) for variations of the HD0.1 run with different  $T_{\text{ff}}$ . In general, higher minimum temperatures lead to less fragmentation and a more stable main clump but the evolution is not linear with  $T_{\text{ff}}$ .

but results converge for minimum temperatures of  $T_{\text{ff}} \leq 10^3$  K. As a result of this speed-up in condensation for low values of  $T_{\text{ff}}$ , by  $5 t_{\text{cc}}$ , the highest and lowest  $T_{\text{ff}}$  have a similar amount of total cold gas mass, while the intermediate-floor runs have a smaller amount.

The evolution in warm gas mass, shown in Fig. 9, is similarly non-linear. Again the early evolution is directly dependent on the cooling floor temperature  $T_{\text{ff}}$ , with lower  $T_{\text{ff}}$  producing less warm gas for  $t < t_{\text{cc}}$ . For later times, the long-term evolution of the total warm gas mass  $M_w$  is generally a function of  $T_{\text{ff}}$ , with higher  $T_{\text{ff}}$  producing less  $M_w$ . The outlier to this trend is HD0.1\_F5.0, which despite having the second highest  $T_{\text{ff}}$  produces a similar amount of  $M_w$  as runs with  $T_{\text{ff}} \leq 10^{3.5}$  K.

This somewhat complex behaviour in the warm phase is due to how cloud shattering proceeds for each simulation. As can be seen in Fig. 10, the cloud evolution changes fundamentally with increasing  $T_{\text{ff}}$ . For low values of  $T_{\text{ff}}$  we see an evolution very similar to that shown for HD0.1 in Fig. 5: the original cloud shrinks rapidly very early on as it loses pressure support, and breaks up into a large number of individual clumps. During this time, the total cold gas mass increases, but the mass of the most massive clump  $M_{\text{min}}$  actually reduces over time as shattering progresses. This occurs within half a crushing time-scale and produces small clumplet fragments, which interact with the wind over the next few crushing times to produce individual, but often connected, wakes of warm gas. This process has been found recently in other studies too, notably by McCourt et al. (2018) and Gronke & Oh (2020b), though Jennings & Li (2021) note that it is still uncertain as to whether fragmentation is shock induced due to the Richtmyer–Meshkov instability (Meshkov 1972), or if some other process is at play, such as pressure interactions between two neighbouring clouds.

For higher  $T_{\text{ff}}$ , the shattering is less strong and the number of individual clumps remains much lower. This produces less mixed gas before  $0.5 t_{\text{cc}}$  as a result of hot gas not being pulled violently into a mixing layer by the pressure gradients during the collapse. In general, higher  $T_{\text{ff}}$  means a more intact main clump with a higher mass (see

evolution of the mass of the most massive clump,  $M_{\text{mm}}$ , in Fig. 10). For the highest values of  $T_{\text{fl}}$  tested here, the main clump remains intact and actually grows in mass over time. The cooling floor temperature has such an important impact because the initial cooling of the cloud, once placed in the ICM, occurs rapidly enough that it is essentially isochoric, which means that the pressure gradient produced at the boundary is linearly proportional to the value of the temperature floor where the cloud settles, and so there is a range of orders of magnitude between the forces these clumps experience across runs. We also note that the number of clumps after the initial ablation event is closely linked to  $l_{\text{cloudlet}}$  shown in Fig. 1: runs with  $T_{\text{fl}}$  corresponding to maxima of  $l_{\text{cloudlet}}$  (e.g. HD0.1\_F5.5 or HD0.1\_F4.0) have less clumps early on than those corresponding to local minima (such as HD0.1\_F4.5 or HD0.1\_F5.0).

After reaching an initial equilibrium, the clouds at the higher temperature floor tend initially to *ablate* more than mix, with clumplets breaking or shredding off from the main clump, increasing the effective mixing surface, and generating mixed gas at the boundary layer. This is perhaps a more traditional cloud-crushing scenario, and one that approaches the behaviour in the no-cooling limit case. Mixed gas does condense to form new cold gas, but the physical extent of the wake at very high temperature floors appears to be suppressed, and there is a larger consolidated ‘head’ of the cloud that remains in the wind.

The amount of ablation and shattering is directly related to the amount of warm gas produced, as can be seen by studying the outlier simulation HD0.1\_F5.0, which produces many more individual clumps around  $1.5 t_{\text{cc}}$  than either HD0.1\_F5.5 or HD0.1\_F4.5. This early ablation event is also the exact point in time when the warm gas mass  $M_w$  for this simulation increased significantly in Fig. 9.

We conclude that internal heating mechanisms could play an important role in the long-term evolution of cold clouds by suppressing ablation and shattering, and allowing the main cloud to survive for longer. However, in a cluster environment, mixing at the cloud surface remains sufficiently efficient that even with reduced shattering clouds grow in mass over time, albeit slower than those that originally, were originally mixed more efficiently into the warm phase.

#### 4.1.4 Kelvin–Helmholtz versus pressure gradients

The generation of a mixed phase at the boundary layer of the cloud is the key process that drives the evolution and long-term growth of the clouds via condensation in our simulations. Gronke & Oh (2020a), who find robust cloud growth in a galactic setting, argue that rapid cooling can generate pressure gradients large enough that mixing in the boundary layer is dominated by pressure-driven mixing rather than by Kelvin–Helmholtz processes in the shear layer. If pressure mixing dominates, the cooling rate directly determines the growth rate of the cloud, and growth continues even when the cloud is almost comoving.

To understand how mixing proceeds in our simulations, we plot the growth rate of the cold gas fraction normalized to the current cold mass  $\dot{M}_c/M_c$  against the velocity of the cloud (which is initially at rest in the simulation frame) in Fig. 11. Note that ‘cloud’ refers to the entire wake of mixed gas, not the most massive remnant of the original cloud. As can be seen in Fig. 10, the most massive clump loses mass over time, and therefore has a *negative* growth rate, while the cloud has *positive* growth rate as the total gas mass increases over time. Random motions not along the axis of flow are included in this root-mean-square velocity, since this velocity dispersion can

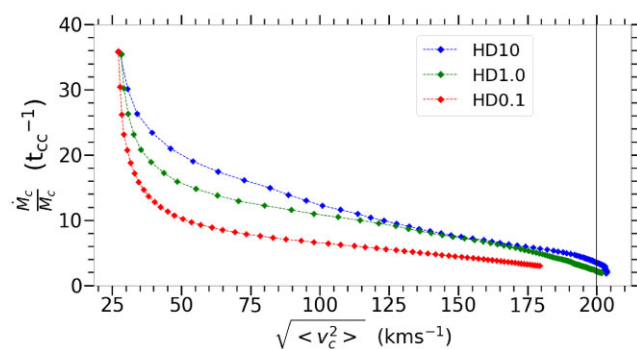


**Figure 11.** The root-mean-square velocity of the cold gas against the growth rate of the cold cloud, normalized to the total cold mass in the box at the present time for each data point, in units of  $t_{\text{cc}}^{-1}$ , for our three hydro runs. The initial collapse and shattering phase is not included. Note that the mean-square velocity of the cloud relative to its *initial* zero velocity is plotted, and that the wind velocity sits at  $200 \text{ km s}^{-1}$ . The mass-normalized growth rate reduces as the cloud becomes comoving in the wind, indicating that the mixing is largely Kelvin–Helmholtz instability driven and that the rate of condensation onto the cloud reduces as the cloud decelerates and the Kelvin–Helmholtz mixing becomes less effective.

still contribute to instability mixing, although in practice the velocity magnitudes are in general small compared to the bulk flow. (This can be seen by only a small excess velocity of the gas in the approximately comoving state reached by HD1.0 and HD10.)

We find that though the total cloud growth rate continues to increase with time as the cloud becomes approximately comoving with the wind, the normalized rate – which takes into account the fact that at later times the cloud is larger and has a greater mixing area – reduces. For example, when the overall cloud reaches approximately comoving status, the normalized growth rate is around 5–10 per cent the value at a relative velocity of  $170 \text{ km s}^{-1}$ . This supports the argument that the condensation and cloud growth is driven by Kelvin–Helmholtz mixing, which acts to a lesser extent when the cloud slows down relative to the wind, rather than the pressure mixing. In the growth rate of the warm fraction (not shown), we see a similar decline as the cloud becomes comoving, but a peak in growth rate between  $75$  and  $100 \text{ km s}^{-1}$ ; most likely this corresponds to the point where the cold gas area becomes completely covered in a warm mixing layer.

In clusters this slowing down occurs due to both the ram pressure experienced by the cloud gas as it punches through the ICM, and also due to the gravitational effect of the cloud climbing out of the central potential in the cluster. The cloud can also slow down/become entrained due to cooling gas imparting momentum to the cloud as it condenses. Treating this case as an inelastic collision and conserving momentum, the approximate velocity relative to the wind at a given time will be  $\frac{\Delta v(t)}{v_{\text{wind}}} \approx \frac{m_{\text{cl},0}}{m_{\text{cl}}(t)}$  (Gronke & Oh 2018).

## 4.2 Magnetic fields and cloud growth

Observational studies of galaxy clusters using fast radio burst (FRB) probes (e.g. Prochaska et al. 2019) and rotation measures (e.g. Farnes et al. 2017; Malik, Chand & Seshadri 2020) have shown that the ICM is magnetized with a field strength of about  $2 \mu\text{G}$ . However, field strengths in the centres of cluster cooling flows may be an order of magnitude higher (see Carilli & Taylor 2002), and recent observations of the Smith cloud (a high velocity cloud around 3 kpc below the galactic plane of the Milky Way with a size and temperature comparable to our simulated clouds) by Hill et al. (2013) and Betti

et al. (2019) give lower bounds on the peak line-of-sight field strength of 8 and 5  $\mu\text{G}$ , respectively. Magnetic fields have long been assumed to be dynamically unimportant in the cloud-crushing problem, with the magnetic pressure often orders of magnitude lower than the thermal pressure. However, with mixing being recognized as the dominant mechanism for cloud evolution, more and more simulations of the CGM and ICM have begun to consider their effect in recent years. Such simulations have shown that magnetic fields can help prevent shredding by stabilizing perturbation modes aligned with the field (via draping, see e.g. Mac Low et al. 1994; McCourt et al. 2015; Sparre et al. 2020), and by establishing anisotropic thermal conduction (e.g. McCourt et al. 2012; Jennings & Li 2021), with draping then able to suppress conduction across the boundary layer (Dursi & Pfrommer 2008).

In this section, we investigate how magnetic fields of different strengths and orientations influence the evolution of cold clouds as they travel through the hot ICM. The additional impact of thermal conduction will be studied in Section 4.3. Magnetic fields of initial strength  $B$  were initialized in one of two configurations: either *aligned* ('parallel') with the direction of flow, or *normal* ('perpendicular') to the direction of flow. We test three different field strengths, with detailed information on parameter choices for magnetized simulations given in Table 2. All simulations presented in this section and the next are magnetized variations of the HD10 simulation.

As can be seen in Fig. 12, magnetic fields have a significant impact on the morphology of cold clouds and their wake over time, but not enough impact to prevent the growth of the cold cloud mass (see Fig. 13). In comparison to the reference simulation HD10, mass growth is slower for all magnetic field strengths tested here, and this suppression is greater for stronger magnetic fields irrespective of the initial field configuration. The warm gas mass fraction is similarly suppressed, as shown in Fig. 14, with initially stronger magnetic fields leading to less warm gas mass. Interestingly, the trend in mass growth is not reversed between the warm and cold gas phases like it is for the simulations of clouds with different density (see Section 4.1.2), where the clouds that grow fastest in cold gas mass tended to generate the least warm gas.

We also see a distinct difference in cloud evolution between the two magnetic field configurations tested here, with the perpendicular field suppressing mixing and allowing for more efficient cooling at all field strengths tested than the equivalent runs with initially aligned fields to the flow. For our highest field strength (5  $\mu\text{G}$ ), there is a difference of approximately 8 per cent in the cold gas mass and a difference in the warm fraction of approximately 53 per cent at  $3 t_{\text{cc}}$  between the normal and aligned configurations. For a 1  $\mu\text{G}$  field these differences are larger at  $3 t_{\text{cc}}$ , at 110 per cent and 238 per cent in the cold and warm fractions, respectively. Under the assumption that mixing is driven by the Kelvin–Helmholtz instability, such as in the analytical solution by Chandrasekhar (1961), this trend is surprising. If mixing is instability driven, a magnetic field with field lines parallel to the fluid flow should stabilize the Kelvin–Helmholtz instabilities and slow the growth rate of unstable modes, with larger field strengths providing greater stabilizing action. This is due to the magnetic tension force resisting the bending of field lines.

To explain the trends in the warm gas reported here, it is necessary to instead consider the morphology of the cloud and the topology of the field lines that result from the two initial field set-ups. The impact of magnetic fields on the warm gas in particular can be seen visually in Fig. 12, which shows that at fixed field strength, the aligned configuration produces a significantly more extended wake than the normal configuration. This trend is confirmed in Fig. 15 that

shows that at fixed field strength, there are fewer individual fragments downstream in the wake than for magnetic fields perpendicular to the flow. As discussed in Section 4.1.3, a more extended wake and greater fragmentation leads to a greater surface area of interface between the cold and hot gas, which increases mixing and production of the warm phase. This, in turn, drives increased condensation.

There are several mechanisms suppressing the wake in the perpendicular field configuration. First, there is a strong magnetic draping effect taking place near the head/s of the clump/s, such as that described by Dursi & Pfrommer (2008) and more recently by Sparre et al. (2020). As the clump moves through the hot ICM, it 'sweeps up' magnetic field lines, which become pinched together near the head of the cloud. Dursi & Pfrommer (2008) find that the magnetic tension associated with this draped layer can dominate over hydrodynamic drag forces in slowing the clump down and reducing fragmentation. Draping of the field does not happen as significantly in the case where the magnetic field is parallel to the flow velocity, since the cloud material can slip along with the field lines. In our case, magnetic draping is present at the head of the cloud, as can be seen by the increased field magnitude at the head of the clumps in the perpendicular field configuration in Fig. 12. Perhaps the most important draping effect however is the suppression of Kelvin–Helmholtz instabilities when the field is tangled, which is not as pronounced if the field is uniform. This is due to a draping layer that suppresses Kelvin–Helmholtz instabilities (Sparre et al. 2020), which is more effective in a tangled-field scenario because in a uniformly magnetized wind the instabilities are suppressed only along the axis that is parallel to the field orientation, rather than along all axes.

The second process acts on the wake behind the clump. As can be seen in the line-integral convolutions that trace the magnetic field direction in Fig. 12, the field morphology in the wake depends strongly on the initial magnetic field topology. For an initially parallel field, the magnetic field wraps around the cloud and wake, and a field configuration that is mostly parallel to the flow is maintained. In the perpendicular case, however, the field becomes very turbulent downstream of the wake. This tangling of the field lines creates magnetic tension, which prevents the wake from elongating as efficiently in the perpendicular field case, due to the Lorentz force on the plasma in this region. This effect is probably enhanced by the suppression of mixing instabilities by draping, with less clumpy material then being swept downstream in the wake.

To quantify this non-uniformity of the field in the wake and compare between the aligned and perpendicular field configurations, we plot the average curl of the magnetic field in non-wind ( $<10^8$  K) fluid in Fig. 16. We find that the perpendicular field always has a higher mass-weighted average of the magnitude of the  $B$ -field curl than the parallel field case in the mixed gas, by up to a factor of a few. This trend persists at later times as the value of the curl converges.

As discussed in Section 4.1.4, mixing in our simulations is primarily driven by Kelvin–Helmholtz instability, but there is still some growth in the cold phase even when the cloud is approximately comoving, which is likely due to the pressure-driven effects. With an initial plasma  $\beta = 10^3$ – $10^{4.5}$  ( $\beta = 2P_{\text{th}}/B^2$ , where  $P_{\text{th}}$  is the thermal pressure and  $B^2/2$  is the magnetic pressure), magnetic pressure effects are negligible in the hot wind but  $\beta$  naturally decreases as the gas cools until  $\beta < 1$  in the cold clumps (see Fig. 17). The relative strength of magnetic pressure at a given temperature depends on the field configuration. Originally perpendicular fields produce a much wider range of  $\beta$  values at a given temperature in comparison to aligned fields. However, for all simulations tested here, much of the warm gas remains on average dominated by thermal pressure

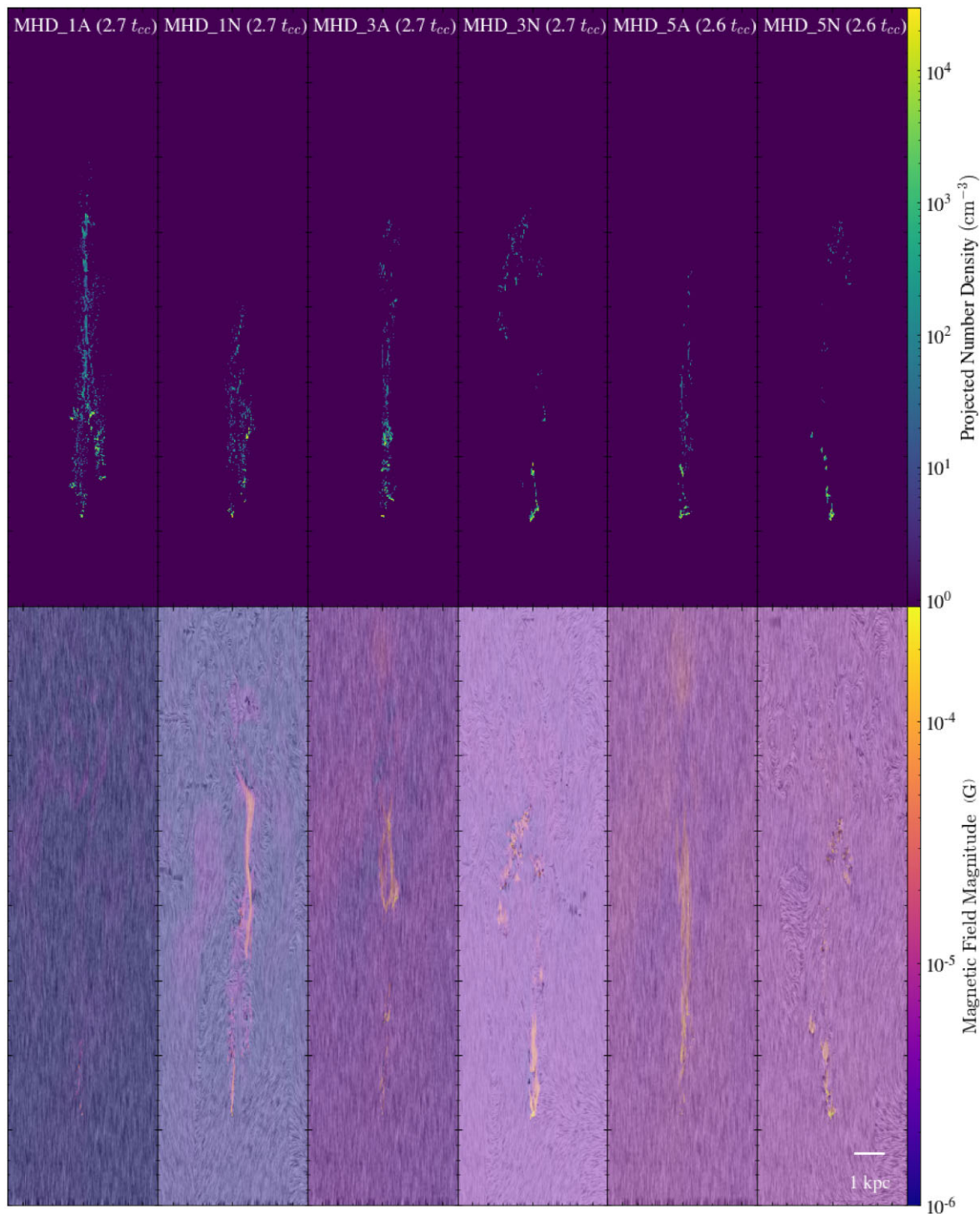


**Figure 12.** The density-weighted projected number density (top panel), and the magnetic field magnitude in a slice of the simulation box for the six MHD only runs. On the lower panels the line integral convolution is plotted to give an idea of the orientation of the magnetic field at each region. One can clearly see that if the field is normal to the flow then the field lines drape more around the head of the cloud, and become more non-uniform in the wake. Also, compared to the no MHD simulations at a similar time (see e.g. Fig. 5 for comparison, though recall that the initial densities are 100 times smaller in the pure hydro plot), the amount of dense, cold gas present is highly suppressed, with higher  $B$  field leading to more suppression.

( $\langle \log(\beta) \rangle \gtrsim 0$ ). The presence of magnetic fields, therefore, does not prevent the pressure-gradient-driven mixing of warm gas into cold gas, and at best merely slows the process down. Interestingly, the minimum  $\beta$  as a function of temperature is the same for both

simulations, but MHD\_3N has a much higher maximum  $\beta$  than gas of the same temperature in MHD\_3A. As a result, all cold clumps are magnetically dominated for MHD\_3A, while some cold clumps remain thermal pressure dominated for MHD\_3N.

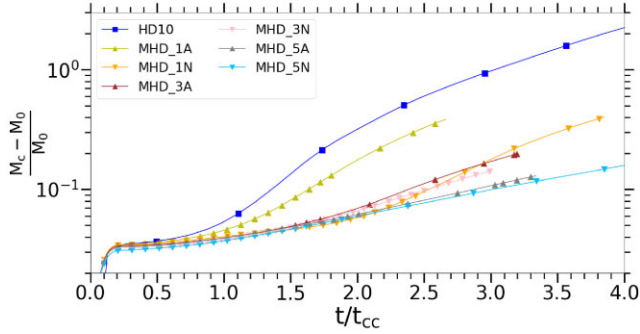


**Figure 13.** Time evolution of the normalized cold gas mass fraction for six magnetized variations of the HD10 simulation, as well as the corresponding hydrodynamical run. Even a weak field suppresses cloud growth, with suppression being stronger for higher field strengths. Magnetic fields initially perpendicular to the flow seem to be more effective at stunting the cloud growth than initially parallel fields, by a larger factor in the 1  $\mu\text{G}$  case and to a lesser extent for stronger field strengths. Note for that for this plot, and all following magnetic field run mass/curl plots, only every fifth data point is shown for clarity.

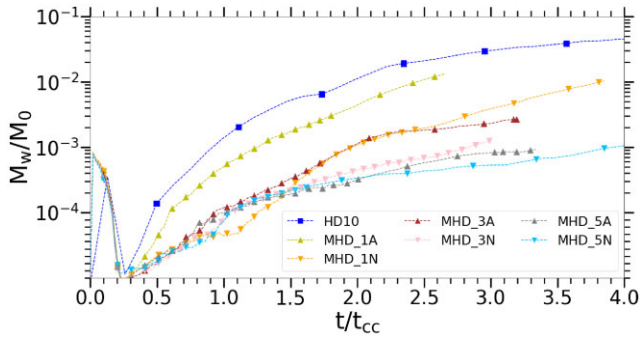


**Figure 14.** Time evolution of the normalized warm gas mass fraction for six magnetized variations of the HD10 simulation. Magnetic fields reduce the amount of warm gas by up to two orders of magnitude over a few crushing time-scales for the range of field strengths tested here. Reduction in the warm gas mass is more pronounced for the simulations where magnetic field lines are initially normal to the flow.

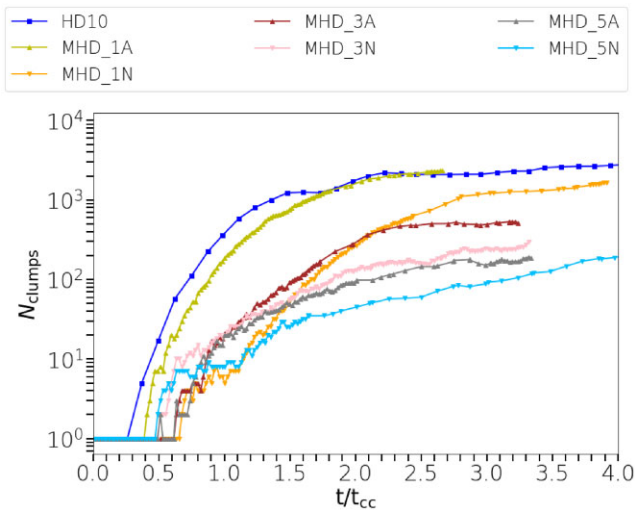


**Figure 15.** Time evolution of the number of clumps (top) for six simulations with different magnetic field orientations and magnetic field strengths of the HD10 simulation. Higher magnetic field strengths, and fields initially orientated normal to the direction of flow, lead to less fragmentation.

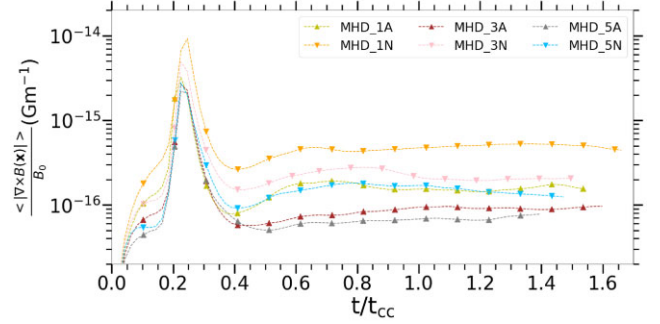


**Figure 16.** The average value of the curl of the magnetic field (mass-weighted) for all ‘non-hot’ gas (i.e. all gas below the wind temperature). The perpendicular field configuration tends to have a larger value of the curl after the early cloud collapse than the parallel field equivalent.

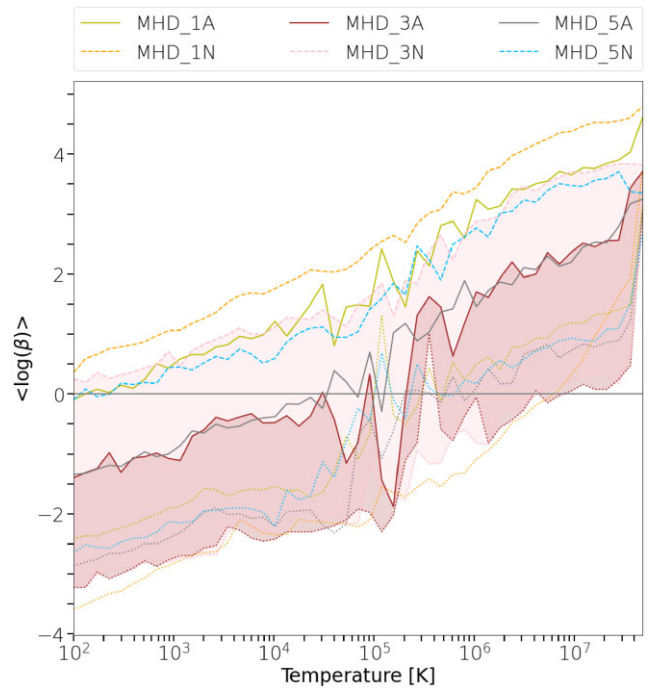


**Figure 17.** Distribution of plasma  $\beta$  versus temperature for all magnetized simulations at  $t = 2.6 t_{cc}$ . Solid (dashed) lines mark the upper 90th percentile of the distribution at a given temperature for all runs with initially parallel (perpendicular) magnetic fields, while dotted lines mark the lower 10th percentile. The shaded regions highlight the range of values for MHD\_3N and MHD\_3A, respectively. Except in the range  $10^5 < T < 10^6$  K, lower limits for MHD\_3N and MHD\_3A are very similar. For runs with an initially perpendicular magnetic field, magnetic pressure support dominates for cold gas, while for initially aligned field the distribution is much wider.

### 4.3 Thermal conduction

In the presence of strong temperature gradients, such as those seen in and around cold clumps in the intracluster environment, free electrons transport heat parallel to the magnetic field lines (Cowie & McKee 1977). This anisotropic thermal conduction is expected to smooth temperature, pressure, and density gradients in multiphase systems (Vieser & Hensler 2007). For sufficiently high field strengths, it will also suppress orthogonal instabilities (e.g. Parrish et al. 2012) as momentum and conductive heat transfer can be restricted almost exclusively to paths along field lines. As well as

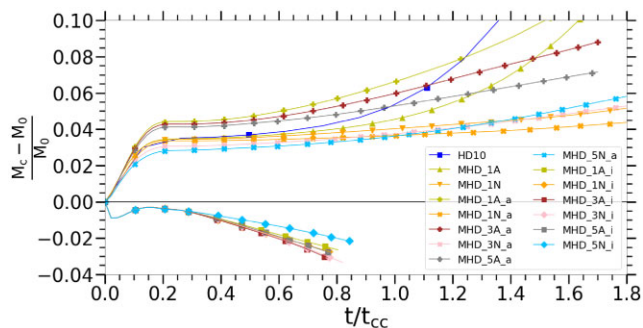


**Figure 18.** Time evolution of the normalized cold fraction for cold clouds simulated with magnetic fields and thermal conduction. Isotropic thermal conduction causes clouds to evaporate in the hot wind, while anisotropic thermal conduction is insufficient to prevent their growth. Note that the growth rate for MHD runs is slow within the first  $t_{cc}$ , hence the linear scale on the vertical axis.

stabilizing instabilities and thus reducing the proportion of the gas in the catastrophically cooling warm phase, conduction has the potential to directly slow down the cloud growth by offsetting radiative cooling losses with energy transferred from the surrounding hot medium.

Anisotropic conduction is computationally expensive to model in simulations and for this reason has frequently been omitted in previous work on the cloud-crushing problem, or approximated using analytic assumptions based on the morphology of the magnetic field, which translates to a numerical ‘fudge factor’ in the classical Spitzer formula (Spitzer 1962). In this paper, we explicitly model the conduction within RAMSES as part of our full MHD set-up. All simulations with conduction are detailed in Table 2, and include runs with either isotropic (post-fixed with  $X_i$ ) and anisotropic conduction ( $X_a$ ). For each type of conduction we test a strong, an intermediate, and a weak field in both the perpendicular and aligned configuration. We shall continue referring to the magnetized runs without conduction as ‘MHD’ runs.

The clearest impact of conduction is seen in the cold gas, where cloud evolution separates into two very distinct modes depending on whether the conduction is isotropic or not (see Fig. 18): isotropic conduction causes the cold gas mass to decrease over time, similarly to but more slowly than what is observed in the non-cooling runs shown in Fig. 3. For all runs with isotropic conduction, the hot ICM can supply sufficient thermal energy to offset cooling and prevent the formation of new cold gas from the mixed phase. The peak in the condensed mass just after  $0.15 t_{cc}$  (where the cold mass losses are briefly almost nullified) is likely due to the high fraction of warm gas formed within  $0.1 t_{cc}$ , which may manage to condense some cold gas before the warm fraction drops after  $0.2 t_{cc}$ . From there on, the cold mass is reduced by around 1 per cent by  $0.4 t_{cc}$  and by 2–3 per cent by  $0.8 t_{cc}$ . This mass-loss rate is around 10 times slower than the non-cooling run of the same density, HD10\_nc whose cold mass is reduced by 30 per cent by  $0.9 t_{cc}$ . We conclude that isotropic thermal conduction is able to offset radiative cooling in and around cold clouds in galaxy clusters and to prevent their growth on long time-scales.

As expected, conduction acts to generally increase the warm gas fraction compared to the MHD runs, due to its ability to transfer heat from the background hot wind to the mixed phase. This is shown in Fig. 19. This warm gas can no longer be classified as a pure ‘mixed’ phase, as heat is now allowed to flow along temperature gradients, i.e. warm gas is now also generated through the heat flux from the hot ICM into the cold cloud fluid. As a result, more warm gas is

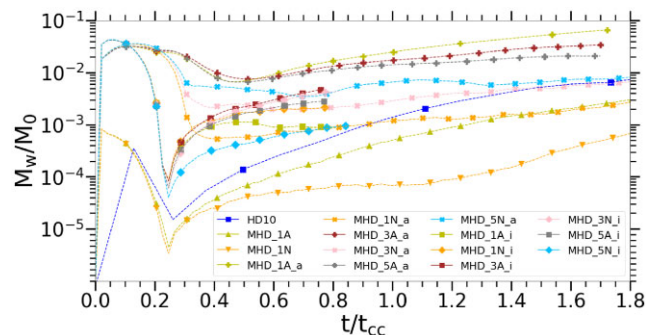


**Figure 19.** The normalized warm mass fraction for all simulations with magnetic fields and thermal conduction. Both isotropic and anisotropic thermal conduction increase the amount of warm gas in comparison to simulations without conduction. This effect is generally stronger for anisotropic than isotropic thermal conduction.

created early on, up to  $\sim 100$  times the amount seen in simulations without conduction at  $0.1 t_{cc}$ , since conduction time-scales are shorter than the dynamical mixing time-scales. The conduction runs produce more warm gas than any of the purely hydrodynamical or MHD runs. For example MHD\_1N\_a and MHD\_1N\_i produce 13 and 37 times as much warm gas, respectively, as MHD\_1N at  $0.6 t_{cc}$ .

The influence of thermal conduction on both the amount of cold and warm gas can be clearly seen in Fig. 20, with isotropic conduction producing significantly wider wakes than anisotropic conduction. While the remaining cloud stays very compact in the isotropic conduction phase, any material ablated is mixed into a wide, turbulent wake that is quickly heated to hot gas temperatures. By contrast, in the anisotropic case, wakes remain much narrower and the ablation of diffuse material from the back of cloud produces the warm gas seen here.

For all anisotropic cases we see evolution more in line with the other simulations presented in this paper: clouds grow in mass over time, as can be seen in more detail in Fig. 21. Apart from an early boost in cold gas mass for the cases with an aligned magnetic field, the growth rate of cold gas in the presence of anisotropic conduction is reduced in comparison to the equivalent non-conducting runs. The impact of anisotropic thermal conduction on both the cold and the warm phase can be understood in the context of the length scales of conduction in and around cold clouds. Following section 3.1 of Li et al. (2020), the heat precursor in the hot phase is  $\lambda_e \simeq 100$  pc. The skin depth of heat conduction in the cloud is  $\lambda_{skin} = \lambda_e / \chi \simeq 1$  pc. As a result, the thermal conduction has no direct effect on the cold cloud (such as suppressing Kelvin–Helmholtz instabilities or reheating cold gas to the warm phase), but it warms up the mixing layer on a 100 pc scale. This leads to the increased amount of warm gas observed here, but also explains why this warm gas cools more slowly into cold gas. Note that the effect of thermal conduction is directly proportional to density of the cloud. For clouds with  $\chi < 100$  the skin depth will quickly increase, and thermal conduction should have a very significant effect on the cloud structure and the number of cloudlets.

To understand the early boost in cold gas mass for aligned magnetic fields in the presence of anisotropic thermal conduction (compare MHD\_1A\_a to MHD\_1A and MHD\_1N\_a in Fig. 21), one needs to look in detail at where anisotropic conduction extracts the energy from the hot wind. As can be seen visually in Fig. 22, in the aligned case (MHD\_1A\_a), thermal energy is extracted upstream of the cloud as it flows down the magnetic field lines. This creates a cooler plume of gas ahead of the cloud, which, due to the loss of thermal pressure,

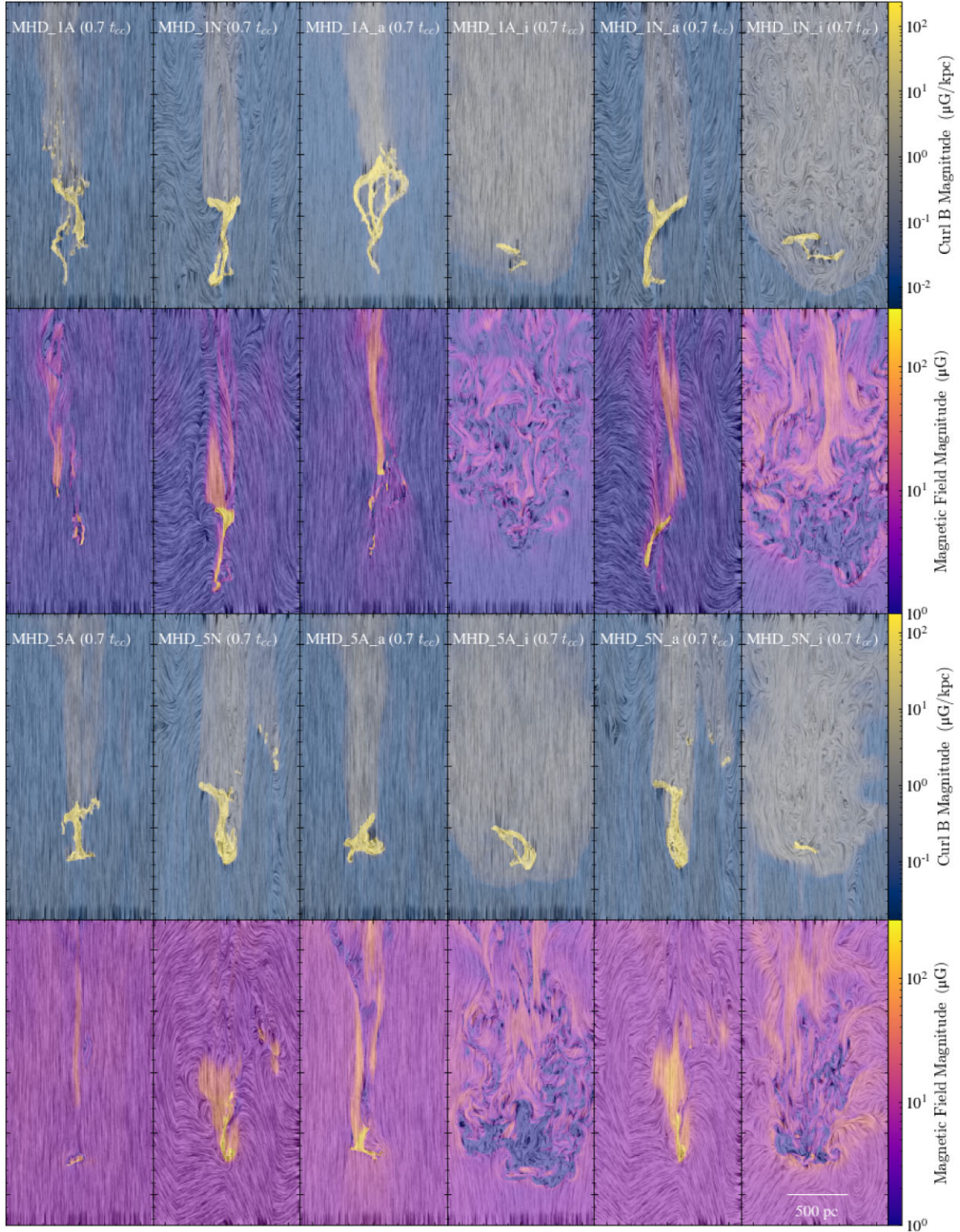


**Figure 20.** The density-weighted magnetic curl projection (top panel) and magnetic field magnitude slice (bottom panel) for the eight MHD runs with thermal conduction, as well as four corresponding non-conduction MHD runs. The orientation of the magnetic field lines is shown via the line integral convolution.

also becomes somewhat denser. Because of the flow direction, this gas then impact the mixing layer of the cloud, where the early cooling at  $t < 0.2 t_{cc}$  occurs. With a perpendicular magnetic field (MHD\_1N\_a in Fig. 22), a similar plume forms next to the cloud but due to its location, the plume in this case flows downstream without

interacting further with the cloud. For this reason, the cloud in the aligned case is fed by pre-cooled, denser gas early on which reduces the cooling times in the mixing layer. By contrast, the cloud in a perpendicular field configuration is fed by pristine wind gas, like in the non-conducting case. As a result, clouds in an aligned field

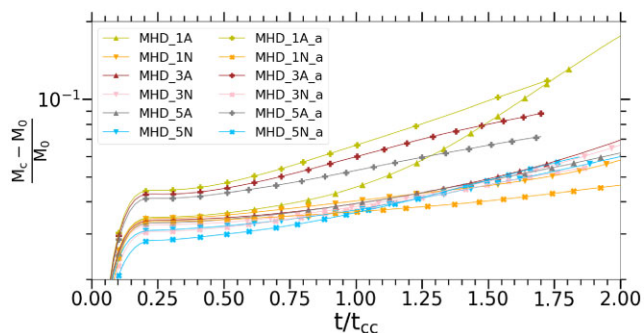


**Figure 21.** Time evolution of the normalized cold fraction for all cold clouds that grow in Fig. 18. Anisotropic conduction makes little difference to the evolution of the cloud for a magnetic field that is normal to the direction of flow, but boosts the growth of cold gas for an initially aligned magnetic field.

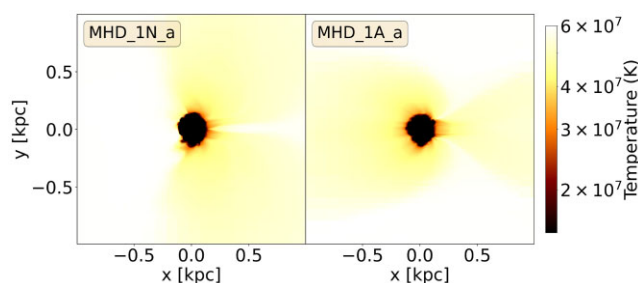


**Figure 22.** Slice plot of the temperature in MHD\_1N.a (left) and MHD\_1A.a (right) at  $t = 0.18 t_{cc}$ . Limits were chosen to highlight the structure of the plume pre-cooled by thermal conduction.

configuration grow faster. We expect this early boost to cold gas mass to be almost entirely restricted to magnetic fields parallel to the flow. In most other configurations, magnetic field lines will quickly drape over the cloud (see Sparre et al. 2020, for a careful study of draping), suppressing conduction at the surface and maintaining large temperature gradients with reduced ‘mixing’. Heat transport would also be restricted to chaotic paths in the tangled field, which may further reduce the efficiency of heat transfer and the mass fraction of the warm phase.

From our simulations with thermal conduction, it is clear that conduction adds significant complexity to the problem of cloud growth; on one hand, heat conduction from the wind to the boundary layer increases the warm fraction, which, in turn, can increase the growth depending on where the pre-cooled gas is located. Conversely, the same conduction channel can supply heat from the wind to this warm fraction (whether generated by conduction or Kelvin–Helmholtz mixing), and help to offset radiative losses, increasing the cooling time-scale and consequently decreasing the condensation rate. However, we find that with anisotropic thermal conduction, and a range of different magnetic field morphologies, cold clouds in the hot ICM continue to grow, albeit more slowly than in the non-magnetic case.

We do note that the magnetic field and conduction runs are very computationally expensive, and as such we are only able to push them to a few crushing times at most. This may mean that we miss important late-stage evolution while the cloud is entrained, which could be different to the early stage evolution where the cloud is mainly being mixed and accelerated and generates a ‘tail’ (see e.g. Grønnow, Tepper-García & Bland-Hawthorn 2018; Gronke & Oh 2020a; Kanjilal et al. 2021). This entrainment phase usually starts

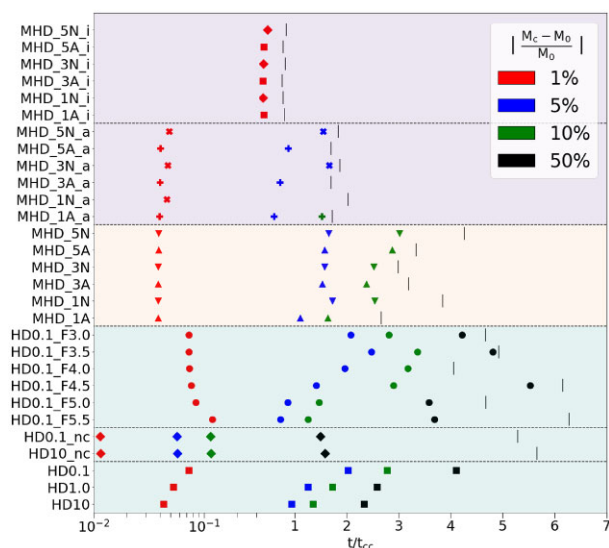


**Figure 23.** Time it takes for clouds to increase (or decrease, in the case of no-cooling or isotropic conduction) their cold gas mass by 1 per cent, 5 per cent, 10 per cent, and 50 per cent. Where necessary, the time was linearly interpolated between existing simulation outputs. All MHD simulations are variants of HD10. General trends that have been described in detail in previous sections stemming from the effects of magnetic fields, various cloud densities, and differing temperature floors can be easily seen. The  $x$ -axis is logarithmic up to  $t/t_{cc} = 10^{-0.5}$  and linear thereafter. The vertical black markers show the final time reached for each run.

later for clouds in magnetic fields, and begins after multiple  $t_{cc}$ , possibly beyond the time we are able to simulate for our clouds. We therefore advise that while our results apply to the initial stages of cloud growth, without simulations able to follow the late-time evolution of magnetic field and conduction runs one should be cautious to apply the same findings to the latter stages of cloud evolution.

## 5 DISCUSSION AND CONCLUSIONS

In this work, we have performed high-resolution simulations of 500 pc-scale cold clouds in a hot ICM environment. We have gradually introduced an increasingly more complex physical picture, by including radiative cooling, small-scale reheating, magnetic fields with different topologies and strengths, and (anisotropic) thermal conduction, and investigated the impact of each individually, with the aim of better understanding the evolution of cold gas within a cluster environment.

Using a set of cloud parameters typical of fragmented filaments in the realistic hot ICM, we confirm that radiative cooling is the dominant physical process that determines the continued evolution of clouds on tens of Myr time-scales. Except for those simulations with deliberately unphysical models (no cooling or isotropic thermal conduction), our cold cloud grows in mass for all parameters probed here. However, as can be seen in Fig. 23, how fast the cold cloud mass grows is strongly a function of the detailed physics being modelled. The same is true for the warm gas mass, as summarized in Fig. 24. Specifically our findings are as follows.

- (i) The presence of radiative cooling breaks the scale-free nature of the cloud-crushing problem, by introducing an additional characteristic time-scale that depends on cloud density, temperature, and metallicity.

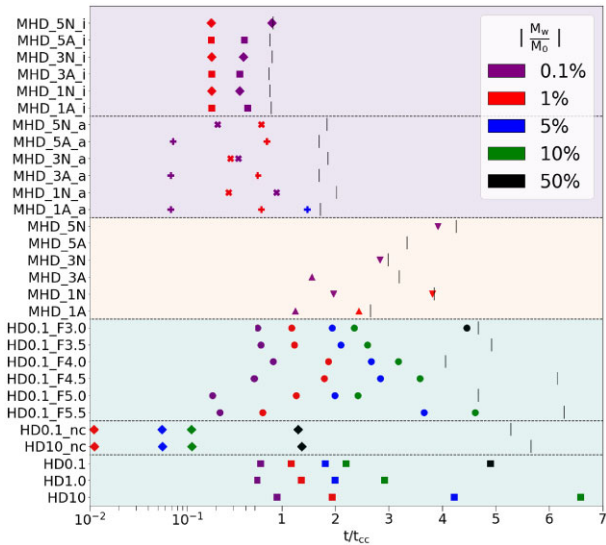


**Figure 24.** Time it takes for clouds to increase (or decrease, in the case of no-cooling or isotropic conduction) their warm gas mass by 1 per cent, 5 per cent, 10 per cent, and 50 per cent. Where necessary, the time was linearly interpolated between existing simulation outputs. The bottom axis is logarithmic up to  $t/t_{cc}=10^{-0.5}$  and linear thereafter. The vertical black markers show the final time reached for each run.

(ii) Because of radiative cooling in the warm phase, cold clouds can significantly increase their mass on cloud-crushing time-scales, as the dynamical generation of the warm phase via Kelvin–Helmholtz instabilities is the limiting factor for growth. We find a drop-off in cloud growth as the cloud starts to become comoving with the wind, as mixing is driven mainly by Kelvin–Helmholtz instabilities rather than pressure gradients induced by cooling.

(iii) As expected, initially denser clouds show faster mass growth due to the more rapid condensation of gas from the warm to the cold phase. Lower density clouds form lower density fragments post-shattering, and this results in greater mixing of cold gas into a warm phase.

(iv) The exact minimum temperature to which the cloud can cool (the temperature floor) splits the cloud evolution into two modes, which we link to theoretical predictions of post-shattering clump length scales: above a certain temperature ( $\sim 10^4$  K) the cloud ablates in the wind, with clumplets being formed dynamically and a significant cloud ‘head’ retained. Instead for low-temperature cooling, the cloud shatters due to cooling-induced pressure instability, forming many fragments, and takes more time to start generating warm gas. We therefore conclude that care must be taken to model low-temperature cloud cooling, which should be ideally tuned to observations and/or well-motivated models of subcloud heating.

(v) Adding magnetic fields has little impact on the early evolution of the cold cloud mass but significantly reduces the amount of warm gas in the wake. This is due to the fact that magnetic fields suppress the mixing of gas in the wake of the cloud that occurs even for the weakest  $B$ -fields explored here ( $1 \mu\text{G}$ ). Higher  $B$ -field strengths are most efficient at suppressing cold cloud mass growth and the amount of warm phase.

(vi) The combined effects of magnetic pressure and magnetic tension act to keep the hot and cold/warm phases separate at the boundary layer and reduce the mixing efficiency of the Kelvin–Helmholtz instabilities. Interestingly, the suppression of cloud growth is most pronounced for the field line configuration that is

initially perpendicular to the wind. This stems from the fact that these  $B$ -fields drape around the head of the cloud, increasing their stabilizing effect in the surface layer. Also, the wake region becomes highly disordered, which reduces the effective surface area of the cloud relative to the case where the  $B$ -fields are initially aligned with the flow.

(vii) If isotropic, thermal conduction can deposit sufficient heat from the hot ICM into the cold and warm phases to prevent gains in the cold mass. In this case, the cloud evolution follows a destruction mode evolution that more closely resembles the traditional no-cooling cloud-crushing solution, although at a rate around an order of magnitude slower.

(viii) If the conduction is anisotropic the cloud instead grows similarly to the non-conduction hydrodynamic and MHD runs because the efficiency of heat transport via electrons is greatly reduced. The ICM is then unable to efficiently heat the cold cloud. Thermal losses via radiative cooling in the warm gas dominate again, albeit on a slower time-scale than without conduction.

(ix) This has important implications for both the ICM and other environments: simulations that either do not include magnetic fields or else do not explicitly model the conductive heat flux will not accurately account for changes to the heating efficiency caused by the specific orientation of the magnetic field lines. The presence of a magnetic field in any orientation, even if at the lower end of galaxy cluster values, will prevent conduction from destroying cold clouds.

(x) Anisotropic thermal conduction can give early cold gas production a boost, if the magnetic field is aligned with the flow. Otherwise, the cold gas mass evolution behaves very similarly to the non-conducting case. In both cases, the amount of warm gas is significantly increased even in comparison to the non-conducting, and even the non-magnetic case, as warm gas is created both through mixing and through hot gas that loses thermal energy through conduction.

In general, we find that both modes of evolution (whether ablation from the surface of the cloud, or shattering of the original cloud into smaller cloudlets) impact the long-term evolution of the total cold gas mass. Another important driver, not surprisingly, is the total amount of warm gas produced in and around the cloud. This, in turn, depends on the mixing efficiency in the wake of the cloud, as well as on the efficiency of reheating such mixed gas via thermal conduction. We conclude that adding magnetic fields and anisotropic thermal conduction does not change the overall behaviour of cold clumps, but the relevant time-scales do change, as well as the morphology of the mixed wake.

The growth of the clouds and the further fragmentation of the original parent clump may have important implications for the nature of the cold clump accretion (Gaspari et al. 2013) onto the central BCG. The shattering and/or ablation of cold clouds, as well as the growth in the cold mass, could alter the evolution of the cluster as a whole. Our results are also an important consideration when attempting to explain the so-called cooling flow problem, whereby feedback processes from the central AGN in the galaxy cluster are theorized to heat cold gas to observed levels, and prevent cooling of hot gas. We find that the cold gas mass in our simulations can grow by a factor of 10 within a few 100 Myr (although other cluster processes that we have not explicitly modelled would be expected to also affect cloud evolution on these time-scales). Any proposed heating mechanism within clusters should be able to explain the observed cooling times and gas temperatures whilst also taking this extra cold mass into account.

We note that the cluster parameter space is very large, and so it is difficult in practice to build a wholly comprehensive picture of cloud evolution in these systems through simulations that cover the entire range of free parameters. Instead, we have presented detailed studies for a typical fragment as those seen in the cluster-scale hydrodynamic simulations of Beckmann et al. (2019) and the magnetized version of the same cluster discussed in Beckmann et al. (2022a,b). For our simulated cloud, we have found robust general trends governing cloud evolution under increasingly complex physics, such as magnetic fields and thermal conduction, and have shown that even with magnetic fields and thermal conduction, the continued evolution of individual cold clouds cannot be ignored when studying the cooling flow problem of galaxy clusters.

## ACKNOWLEDGEMENTS

FJ developed code, ran simulations, analysed data, interpreted results, and wrote the manuscript. RSB initiated the project, developed code, analysed data, interpreted results, and wrote the manuscript. DS and YD interpreted results, provided discussion, and edited the manuscript. We would like to thank the referee, Professor Peng Oh, for a constructive referee report that improved the paper. FJ and RSB thank Newnham College, Cambridge, for financial support. This work was supported by the ERC Starting Grant 638707 ‘Black holes and their host galaxies: co-evolution across cosmic time’ and by STFC. This work was performed using resources provided by the Cambridge Service for Data Driven Discovery (CSD3) operated by the University of Cambridge Research Computing Service ([www.csd3.cam.ac.uk](http://www.csd3.cam.ac.uk)), provided by Dell EMC and Intel using Tier-2 funding from the Engineering and Physical Sciences Research Council (capital grant EP/P020259/1), and DiRAC funding from the Science and Technology Facilities Council ([www.dirac.ac.uk](http://www.dirac.ac.uk)). DiRAC is part of the National e-Infrastructure.

## DATA AVAILABILITY

The data used in this work may be shared on reasonable request to the corresponding author.

## REFERENCES

Allen S. W., Fabian A. C., 1998, *MNRAS*, 297, L63  
 Armillotta L., Fraternali F., Marinacci F., 2016, *MNRAS*, 462, 4157  
 Baumgartner W. H., Loewenstein M., Horner D. J., Mushotzky R. F., 2005, *ApJ*, 620, 680  
 Beckmann R. S. et al., 2019, *A&A*, 631, A60  
 Beckmann R. S., Dubois Y., Pellissier A., Olivares V., Polles F. L., Hahn O., Guillard P., Lehnert M. D., 2022a, *A&A*, 665, A129  
 Beckmann R. S., Dubois Y., Pellissier A., Polles F. L., Olivares V., 2022b, *A&A*, 666, A71  
 Begelman M. C., Fabian A. C., 1990, *MNRAS*, 244, 26P  
 Betti S. K., Hill A. S., Mao S. A., Gaensler B. M., Lockman F. J., McClure-Griffiths N. M., Benjamin R. A., 2019, *ApJ*, 871, 215  
 Birzan L., Rafferty D. A., McNamara B. R., Wise M. W., Nulsen P. E. J., 2004, *ApJ*, 607, 800  
 Bleuler A., Teyssier R., Carassou S., Martizzi D., 2015, *Comput. Astrophys. Cosmol.*, 2, 5  
 Bohringer H., Voges W., Fabian A. C., Edge A. C., Neumann D. M., 1993, *MNRAS*, 264, L25  
 Bourne M. A., Sijacki D., 2021, *MNRAS*, 506, 488  
 Bourne M. A., Sijacki D., Puchwein E., 2019, *MNRAS*, 490, 343  
 Brüggemann M., Scannapieco E., 2016, *ApJ*, 822, 31  
 Canning R. E. A. et al., 2014, *MNRAS*, 444, 336

Carilli C. L., Taylor G. B., 2002, *ARA&A*, 40, 319  
 Chandrasekhar S., 1961, *Hydrodynamic and Hydromagnetic Stability*. Oxford Univ. Press, Oxford  
 Churazov E., Forman W., Jones C., Böhringer H., 2000, *A&A*, 356, 788  
 Churazov E. et al., 2012, *MNRAS*, 421, 1123  
 Churazov E., Ruszkowski M., Schekochihin A., 2013, *MNRAS*, 436, 526  
 Cooper J. L., Bicknell G. V., Sutherland R. S., Bland-Hawthorn J., 2009, *ApJ*, 703, 330  
 Cowie L. L., McKee C. F., 1977, *ApJ*, 211, 135  
 Das H. K., Choudhury P. P., Sharma P., 2021, *MNRAS*, 502, 4935  
 DeGraf C., Dekel A., Gabor J., Bournaud F., 2017, *MNRAS*, 466, 1462  
 De Grandi S., Ettori S., Longhetti M., Molendi S., 2004, *A&A*, 419, 7  
 Dubois Y., Commerçon B., 2016, *A&A*, 585, A138  
 Dursi L. J., Pfrommer C., 2008, *ApJ*, 677, 993  
 Edge A., 2001, *MNRAS*, 328, 762  
 Fabian A., 1994, *ARA&A*, 32, 277  
 Fabian A. C. et al., 2000, *MNRAS*, 318, L65  
 Fabian A. C., Johnstone R. M., Sanders J. S., Conselice C. J., Crawford C. S., Gallagher J. S. I., Zweibel E., 2008, *Nature*, 454, 968  
 Farnes J. S., Rudnick L., Gaensler B. M., Haverkorn M., O’Sullivan S. P., Curran S. J., 2017, *ApJ*, 841, 67  
 Ferland G. J. et al., 2017, *Rev. Mex. Astron. Astrofis.*, 53, 385  
 Fielding D. B., Ostriker E. C., Bryan G. L., Jermyn A. S., 2020, *ApJ*, 894, L24  
 Fogarty K. et al., 2019, *ApJ*, 879, 103  
 Frank K. A., Peterson J. R., Andersson K., Fabian A. C., Sanders J. S., 2013, *ApJ*, 764, 46  
 Fromang S., Hennebelle P., Teyssier R., 2006, *A&A*, 457, 371  
 Gaspari M., 2015, *MNRAS*, 451, L60  
 Gaspari M., Churazov E., 2013, *A&A*, 559, A78  
 Gaspari M., Brighenti F., Ruszkowski M., 2013, *Astron. Nachr.*, 334, 394  
 Gronke M., Oh S. P., 2018, *MNRAS*, 480, L111  
 Gronke M., Oh S. P., 2020a, *MNRAS*, 492, 1970  
 Gronke M., Oh S. P., 2020b, *MNRAS*, 494, L27  
 Gronke M., Oh S. P., Ji S., Norman C., 2022, *MNRAS*, 511, 859  
 Grønnow A., Tepper-García T., Bland-Hawthorn J., 2018, *ApJ*, 865, 64  
 Hanasz M., Lesch H., 1998, *A&A*, 332, 77  
 Heckman T. M., Baum S. A., van Breugel W. J. M., McCarthy P., 1989, *ApJ*, 338, 48  
 Hill A. S., Mao S. A., Benjamin R. A., Lockman F. J., McClure-Griffiths N. M., 2013, *ApJ*, 777, 55  
 Hitomi Collaboration et al., 2018, *PASJ*, 70, 9  
 Hofmann F., Sanders J. S., Nandra K., Clerc N., Gaspari M., 2016, *A&A*, 585, A130  
 Hudson D. S., Mittal R., Reiprich T. H., Nulsen P. E. J., Andernach H., Sarazin C. L., 2010, *A&A*, 513, A37  
 Jennings R. M., Li Y., 2021, *MNRAS*, 505, 5238  
 Jimenez-Gallardo A. et al., 2021, *ApJ*, 912, L25  
 Kanjilal V., Dutta A., Sharma P., 2021, *MNRAS*, 501, 1143  
 Klein R. I., McKee C. F., Colella P., 1994, *ApJ*, 420, 213  
 Kravtsov A. V., Borgani S., 2012, *ARA&A*, 50, 353  
 Leccardi A., Molendi S., 2008, *A&A*, 487, 461  
 Li Y., Ruszkowski M., Tremblay G., 2018, *ApJ*, 854, 91  
 Li Z., Hopkins P. F., Squire J., Hummels C., 2020, *MNRAS*, 492, 1841  
 Liu W. et al., 2020, *MNRAS*, 492, 3156  
 Lovisari L., Reiprich T. H., 2019, *MNRAS*, 483, 540  
 McCourt M., Sharma P., Quataert E., Parrish I. J., 2012, *MNRAS*, 419, 3319  
 McCourt M., O’Leary R. M., Madigan A.-M., Quataert E., 2015, *MNRAS*, 449, 2  
 McCourt M., Oh S. P., O’Leary R., Madigan A.-M., 2018, *MNRAS*, 473, 5407  
 McDonald M., Veilleux S., Rupke D. S. N., Mushotzky R., 2010, *ApJ*, 721, 1262  
 McDonald M., Veilleux S., Mushotzky R., 2011, *ApJ*, 731, 33  
 McDonald M., Veilleux S., Rupke D. S. N., 2012, *ApJ*, 746, 153  
 McDonald M., Gaspari M., McNamara B. R., Tremblay G. R., 2018, *ApJ*, 858, 45

- Mac Low M.-M., McKee C. F., Klein R. I., Stone J. M., Norman M. L., 1994, *ApJ*, 433, 757
- McNamara B. R., Nulsen P. E. J., 2007, *ARA&A*, 45, 117
- McNamara B. R., Nulsen P. E. J., 2012, *New J. Phys.*, 14, 055023
- McNamara B. R. et al., 2000, *ApJ*, 534, L135
- McNamara B. R. et al., 2014, *ApJ*, 785, 44
- Malik S., Chand H., Seshadri T. R., 2020, *ApJ*, 890, 132
- Meshkov E. E., 1972, *Fluid Dyn.*, 4, 101
- Miyoshi T., Kusano K., 2008, in Pogorelov N. V., Audit E., Zank G. P., eds, ASP Conf. Ser. Vol. 385, Numerical Modeling of Space Plasma Flows. Astron. Soc. Pac., San Francisco, p. 279
- Mo H., van den Bosch F. C., White S., 2010, *Galaxy Formation and Evolution*. Cambridge Univ. Press, Cambridge
- Mushotzky R. F., Serlemitsos P. J., Smith B. W., Boldt E. A., Holt S. S., 1978, *ApJ*, 225, 21
- North E. V. et al., 2021, *MNRAS*, 503, 5179
- Olivares V. et al., 2019, *A&A*, 631, A22
- Parrish I. J., McCourt M., Quataert E., Sharma P., 2012, *MNRAS*, 422, 704
- Peterson J. R., Fabian A. C., 2006, *Phys. Rep.*, 427, 1
- Peterson J. R. et al., 2001, *A&A*, 365, L104
- Peterson J. R., Kahn S. M., Paerels F. B. S., Kaastra J. S., Tamura T., Bleeker J. A. M., Ferrigno C., Jernigan J. G., 2003, *ApJ*, 590, 207
- Ploekinger S., Schaye J., 2020, *MNRAS*, 497, 4857
- Prochaska J. X. et al., 2019, *Science*, 366, 231
- Randall S. W. et al., 2011, *ApJ*, 726, 86
- Reiprich T. H., Böhringer H., 2002, *ApJ*, 567, 716
- Rosen A., Bregman J. N., 1995, *ApJ*, 440, 634
- Russell H. R. et al., 2014, *ApJ*, 784, 78
- Russell H. R. et al., 2017, *ApJ*, 836, 130
- Ruszkowski M., Yang H.-Y. Y. K., Reynolds C. S., 2018, *ApJ*, 858, 64
- Salomé P., Combes F., 2004, *A&A*, 415, L1
- Salomé P. et al., 2006, *A&A*, 454, 437
- Scannapieco E., Brügger M., 2015, *ApJ*, 805, 158
- Schuecker P., Finoguenov A., Miniati F., Böhringer H., Briel U. G., 2004, *A&A*, 426, 387
- Sijacki D., Springel V., 2006, *MNRAS*, 366, 397
- Simionescu A., Werner N., Urban O., Allen S. W., Ichinohe Y., Zhuravleva I., 2015, *ApJ*, 811, L25
- Sparre M., Pfrommer C., Vogelsberger M., 2019, *MNRAS*, 482, 5401
- Sparre M., Pfrommer C., Ehler K., 2020, *MNRAS*, 499, 4261
- Spitzer L., 1962, *Physics of Fully Ionized Gases*, 2nd edn. Wiley, New York
- Sutherland R. S., Dopita M. A., 1993, *ApJS*, 88, 253
- Talbot R. Y., Sijacki D., Bourne M. A., 2022, *MNRAS*, 514, 4535
- Tanuma S., Yokoyama T., Kudoh T., Shibata K., 2003, *ApJ*, 582, 215
- Teysier R., 2002, *A&A*, 385, 337
- Toro E. F., 2009, in *Riemann Solvers and Numerical Methods for Fluid Dynamics*. Springer-Verlag, Berlin, p. 413
- Tozzi P., Rosati P., Ettori S., Borgani S., Mainieri V., Norman C., 2003, *ApJ*, 593, 705
- Tremblay G. R. et al., 2016, *Nature*, 534, 218
- Tremblay G. R. et al., 2018, *ApJ*, 865, 13
- Turk M. J., Smith B. D., Oishi J. S., Skory S., Skillman S. W., Abel T., Norman M. L., 2010, *ApJS*, 192, 9
- Ubertosi F. et al., 2021, *ApJ*, 923, L25
- Urban O., Werner N., Allen S. W., Simionescu A., Mantz A., 2017, *MNRAS*, 470, 4583
- Vantyghem A. N. et al., 2018, *ApJ*, 863, 193
- Vernaleo J. C., Reynolds C. S., 2006, *ApJ*, 645, 83
- Vieser W., Hensler G., 2007, *A&A*, 472, 141
- Voit G. M., Cavagnolo K. W., Donahue M., Rafferty D. A., McNamara B. R., Nulsen P. E. J., 2008, *ApJ*, 681, L5
- Walker S. A., Sanders J. S., Fabian A. C., 2015, *MNRAS*, 453, 3699
- Werner N., Urban O., Simionescu A., Allen S. W., 2013, *Nature*, 502, 656
- Yang H.-Y. K., Reynolds C. S., 2016, *ApJ*, 818, 181
- Zhang D., Thompson T. A., Quataert E., Murray N., 2017, *MNRAS*, 468, 4801
- ZuHone J. A., Miller E. D., Bulbul E., Zhuravleva I., 2018, *ApJ*, 853, 180

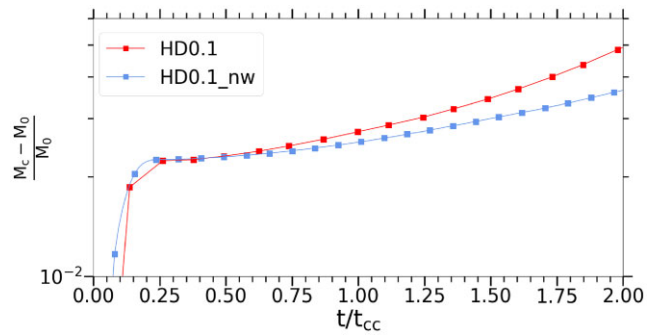


**Figure A1.** Here we plot our fiducial HD0.1 against a no-wind version HD0.1\_nw, for which the only difference is that the wind speed is set to  $0 \text{ km s}^{-1}$ , such that the run models a clump that is initially stationary within the ICM. No significant difference in the cold gas mass growth is seen in the shattering-dominated time-scale  $\lesssim 0.5 t_{cc}$ . Beyond this the wind contribution to mixing starts to dominate and the no-wind run lags behind in mass growth.

## APPENDIX A: RELATIVE CONTRIBUTION OF SHATTERING VERSUS WIND

To investigate the relative contributions to mixing and subsequent cold mass growth from shattering versus wind mixing, we run a version of our flagship cloud HD0.1 with the cloud stationary, in the no-wind run HD0.1\_nw. As expected the mass growth rate post-shattering is reduced in the absence of a wind, as the degree of mixing via fluid instabilities is reduced. The mass growth rate during shattering is similar, and this gives us a measure of the shattering time-scale where cloud collapse and shattering dominates over the contribution from the wind. From Fig. A1 we see that this shattering time-scale is approximately  $0.5 t_{cc}$ .

## APPENDIX B: CONVERGENCE

In this paper, we test a significant range of magnetic field strengths. The computational expense becomes quite large for high-strength fields, where the Alfvén velocity becomes large and the time-step correspondingly small, and also when conduction is modelled. A sensible resolution must therefore be set to make our production runs feasible. Here we would like to test the convergence of our key results when adopting different resolutions for one representative run. The ‘resolution parameter’ that we use in RAMSES is the maximum refinement level LEVEL\_MAX, which gives the number of refinements we allow the grid to make. In a maximally refined grid there will be  $8^{\Delta x - 1}$  leaf (terminal) cells, where  $\Delta x \equiv \text{LEVEL\_MAX}$ . We test the same simulation MHD\_1N (see Section 4.2) with a range of values for LEVEL\_MAX in order to determine the convergence behaviour of our simulations, whilst keeping the minimum refinement level LEVEL\_MIN, which sets the number of cells in the coarse grid, constant. The runs detailed here have a box size of  $(195 \text{ kpc})^3$ , so the maximum spatial resolution is  $195/2^{\Delta x - 1}$ . This is the same as for all non-MHD runs performed in this paper. The MHD and conduction runs have a box-size  $(303 \text{ kpc})^3$  (and also used a LEVEL\_MIN value of 6 as opposed to the value of 5 used for the hydro runs). We plot the change in cold mass for a range of different maximal resolutions below with respect to the lowest resolution simulation (Fig. B1). We find that for times less than  $5 t_{cc}$  there is less cold gas when the resolution of the simulation is increased, however the trend is reversed later on and we expect that our lower resolution simulations are giving us a lower bound on the long-term growth of the cold phase.

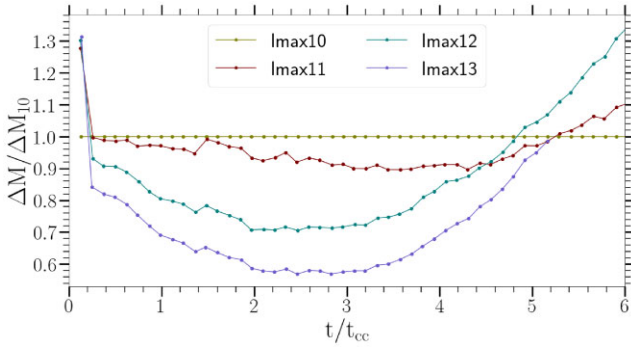


**Figure B1.** The change in cold mass against  $t_{cc}$  for a range of different resolutions for the same simulation run MHD\_1N, with respect to the minimum resolution run that has LEVEL\_MAX equal to 10. While there is an initial paucity of old gas at early times with a higher resolution, this is reversed at around  $5 t_{cc}$ . This indicates that if the resolution were to be increased further, the growth effect we observe should be amplified even more.

This paper has been typeset from a  $\text{\TeX}/\text{\LaTeX}$  file prepared by the author.